Atmospheric
Chemistry
and Physics
Discussions

1   The magnitude of the snow-sourced reactive nitrogen flux to the boundary layer in the

2   Uintah Basin, Utah, USA

3

4   Maria Zatko[1], Joseph Erbland[2,3], Joel Savarino[2,3], Lei Geng[1,a], Lauren Easley[4], Andrew

5   Schauer[5], Timothy Bates[7], Patricia K. Quinn[6], Bonnie Light[8], David Morison[8,b], Hans D.

6   Osthoff[9], Seth Lyman[10], William Neff[11], Bin Yuan[11,12], Becky Alexander[1]

7

8   [1]Department of Atmospheric Sciences, University of Washington, Seattle, 98195, USA

9   [2]Université Grenoble Alpes, LGGE, 38000 Grenoble, France

10   [3]CNRS, LGGE, 38000 Grenoble, France

11   [4]Department of Chemistry, University of Washington, Seattle, Washington, 98195, USA

12   [5]Earth and Space Sciences, University of Washington, Seattle, Washington, 98195, USA

13   [6]Pacific Marine Environmental Laboratory, National Oceanic and Atmospheric

14   Administration, Seattle, Washington, 98115, USA

15   [7]Joint Institute for the Study of the Atmosphere and Oceans, University of Washington,

16   Seattle, Washington, 98195, USA

17   [8]Polar Science Center, Applied Physics Laboratory, University of Washington, Seattle,

18   Washington, 98195, USA

19   [9]Department of Chemistry, University of Calgary, 2500 University Drive NW, Calgary,

20   AB T2N 1N4, Canada

21   [10]Bingham Entrepreneurship and Energy Research Center, Utah State University, 320

22   Aggie Boulevard, Vernal, Utah, 84078, USA

Atmospheric
Chemistry
and Physics
Discussions

Open Access

EGU

23   [11]Cooperative Institute for Research in the Environmental Sciences, University of

24   Colorado, Boulder, Colorado, 80309, USA

25   [12]Chemical Sciences Division, Earth System Research Laboratory, National Oceanic and

26   Atmospheric Administration, Boulder, Colorado, 80305, USA

27   [a]Now at Université Grenoble Alpes, LGGE, 38000 Grenoble, France, CNRS, LGGE,

28   38000 Grenoble, France

29   [b]Now at Department of Physics and Astronomy, University of Utah, Salt Lake City,

30   Utah, 84112, USA

31

32

33

34

35

36

37

38

39

40

41

42

43   Correspondence to Becky Alexander (beckya@uw.edu)

44

45

Atmospheric
Chemistry
and Physics
Discussions

46   **Abstract**

47   Reactive nitrogen (N_r=NO, NO_2, HONO) and volatile organic carbon emissions from oil

48   and gas extraction activities play a major role in wintertime ground-level ozone

49   exceedance events of up to 140 ppb in the Uintah Basin in eastern Utah. Such events

50   occur only when the ground is snow covered, due to the impacts of snow on the stability

51   and depth of the boundary layer and ultraviolet actinic flux at the surface. Recycling of

52   reactive nitrogen from the photolysis of snow nitrate has been observed in polar and mid-

53   latitude snow, but snow-sourced reactive nitrogen fluxes in mid-latitude regions have not

54   yet been quantified in the field. Here we present vertical profiles of snow nitrate

55   concentration and nitrogen isotopes ($\delta^{15}N$) collected during the Uintah Basin Winter

56   Ozone Study 2014 (UBWOS 2014), along with observations of insoluble light-absorbing

57   impurities, radiation equivalent mean ice grain radii, and snow density that determine

58   snow optical properties. We use the snow optical properties and nitrate concentrations to

59   calculate ultraviolet actinic flux in snow and the production of N_r from the photolysis of

60   snow nitrate. The observed $\delta^{15}N(NO_3^-)$ is used to constrain modeled fractional loss of

61   snow nitrate in a snow chemistry column model, and thus the source of snow-sourced N_r

62   to the overlying boundary layer. Snow-surface $\delta^{15}N(NO_3^-)$ measurements range from -

63   5‰ to 10‰ and suggest that the local nitrate burden in the Uintah Basin is dominated by

64   primary emissions from anthropogenic sources, except during fresh snowfall events,

65   where remote NO_x sources from beyond the basin are dominant. Modeled daily-averaged

66   snow-sourced N_r fluxes range from $5.6\text{-}71\times10^7$ molec cm^{-2} s^{-1} over the course of the field

67   campaign, with a maximum noon-time value of 3.1×10^9 molec cm^{-2} s^{-1}. The top-down

68   emission estimate of primary, anthropogenic NO_x in the Uintah and Duchesne counties is

Atmospheric
Chemistry
and Physics
Discussions

Open Access

EGU

69   at least 300 times higher than the estimated snow NO_x emissions presented in this study.

70   Our results suggest that snow-sourced reactive nitrogen fluxes are minor contributors to

71   the N_r boundary layer budget in the highly-polluted Uintah Basin boundary layer during

72   winter 2014.

73

74

75

76

77

78

79

80

81

82

83

84

85

86

87

88

89

Atmospheric
Chemistry
and Physics
Discussions

1. Introduction

90

91   Ozone (O_3) has adverse respiratory effects, is an effective greenhouse gas [*UNEP*, 2011],

92   and, through formation of the hydroxyl radical, influences the oxidizing capacity of the

93   atmosphere [*Thompson,* 1992]. O_3 precursors include volatile organic compounds

94   (VOCs) emitted from vegetation, biomass burning, and fossil fuel combustion [*Guenther*

95   *et al.*, 1995, *Warneke et al.*, 2014] and nitrogen oxides ($NO_x=NO+NO_2$) emitted from

96   fossil fuel combustion, biomass burning, soil microbial activity, lightning, and

97   photochemical reactions in snow [*Delmas et al.*, 1997, *Grannas et al.*, 2007, *Logan et al.*,

98   1983]. Maximum boundary layer O_3 concentrations are typically observed during the

99   summer in major cities, where and when O_3 precursor emissions and ultraviolet (UV)

100   radiation are highest. High O_3 concentrations in the boundary layer exceeding 100 ppbv

101   were measured in winter 2005 in the Upper Green River Basin in rural Wyoming [*Schnell*

102   *et al.*, 2009], well above the current Environmental Protection Agency (EPA) National

103   Ambient Air Quality Standard (NAAQS) 8-hour average limit of 70 ppbv. High

104   wintertime O_3 episodes have also been observed in the Uintah Basin in rural Utah

105   [*Martin et al.*, 2011], and in both basins, these O_3 episodes only occur when the ground is

106   snow-covered [*Oltmans et al.*, 2014]. The Upper Green River Basin and the Uintah Basin

107   are regions of major oil and gas development, and the production of oil and natural gas in

108   the Upper Green River Basin and the Uintah Basin is expected to increase through at

109   least 2020 [*US EIA*, 2014].

110

111   These wintertime high O_3 episodes motivated a series of field campaigns, including the

112   Upper Green Winter O_3 Study (UGWOS 2011, UGWOS 2012) and the Uintah Basin

113   Winter O_3 Study (UBWOS 2012, UBWOS 2013, UBWOS 2014). Results from these

114   field campaigns [*Gilman et al.*, 2013, *Helmig et al.*, 2014, *Oltmans et al.*, 2014, *Warneke*

115   *et al.*, 2014, *Schnell et al.*, 2009] and subsequent modeling studies [*Ahmadov et al.*, 2015,

116   *Carter and Seinfeld*, 2012, *Edwards et al.*, 2013, 2014, *Field et al.*, 2015, *Rappengluck et*

117   *al.*, 2014] reveal that emissions of NO_x and VOCs from oil and gas extraction, combined

118   with stagnant meteorological conditions, enhanced boundary layer UV radiation due to

119   the high UV albedo of snow [*Warren et al.*, 2006], and reduced O_3 loss through surface

120   deposition due to snow cover [*Ahmadov et al.*, 2015], trigger high boundary layer O_3

121   episodes in these basins. O_3 exceedance events occur only when the ground is snow

122   covered because snow aids in the formation and maintenance of a stable air mass and

123   reflects UV radiation upwards into the boundary layer. Modeling studies were used to

124   determine whether O_3 formation in these regions is NO_x-sensitive or VOC-sensitive,

125   which is necessary information for the enactment of effective regulations aimed to reduce

126   boundary layer O_3 abundance. Modeling results from Edwards et al. [2014] suggest that

127   the Uintah Basin is in an O_3 formation regime on the boundary between VOC-sensitive

128   and NO_x-sensitive and modeling results from Ahmadov et al. [2015] suggest that the

129   Uintah Basin regime is VOC-sensitive. Modeling results presented in Edwards et al.

130   [2014] suggest that the dominant radical sources in the Uintah Basin are carbonyl

131   compounds (85%), with smaller inputs from HONO, O_3, and nitryl chloride ($ClNO_2$)

132   photolysis.

133

134   In addition to aiding in the formation and maintenance of a stable air mass with enhanced

135   UV radiation, snow may also recycle reactive nitrogen oxides (N_r = NO_x, HONO)

Atmospheric
Chemistry
and Physics
Discussions

136   between the snow surface and the overlying atmosphere, effectively increasing the

137   atmospheric lifetime of N_r. The major sink of N_r in the atmosphere is the formation and

138   deposition of nitrate (particulate NO_3^- plus $HNO_3(g)$). When nitrate is deposited to snow,

139   its photolysis serves to recycle N_r to the overlying boundary layer [*Grannas et al.,* 2007,

140   *Honrath et al.*, 2000]. This snow-sourced N_r can then be re-oxidized to nitrate and re-

141   deposited to the snow surface. The recycling of nitrogen between the snow surface and

142   boundary layer can occur many times, resulting in the continuous recycling of N_r during

143   sunlit conditions.

144

145   The photolysis of nitrate occurs in the liquid-like region (LLR) in or on ice grains

146   [*Domine et al.*, 2013] in the top snow layer where UV radiation is present, which is

147   known as the snow photic zone. Snow nitrate photolyzes at wavelengths (λ)=290-345 nm

148   to produce aqueous-phase nitrogen dioxide (NO_2) or nitrite (NO_2^-) according to E1 and

149   E2 [*Grannas et al.*, 2007, *Mack and Bolton*, 1999, *Meusinger et al.*, 2014].

150

151    $NO_3^-(aq) + h\nu(+H^+) \rightarrow NO_2(aq) + OH(aq)$,   E1

152    $NO_3^-(aq) + h\nu \rightarrow NO_2^-(aq) + O(^3P)(aq)$,   E2
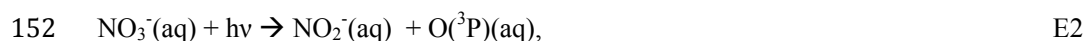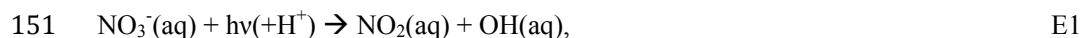
153

154   The measured quantum yields (ϕ) for E1 range from 0.003-0.6 molec photon^{-1} at 253 K

155   [*Chu and Anastasio*, 2003, *Meusinger et al.*, 2014, *Zhu et al.*, 2010], and is likely

156   influenced by the location of nitrate within ice grains. The NO_2 produced in E1 quickly

157   evaporates due to its low solubility and can be transported to the overlying atmosphere.

Atmospheric
Chemistry
and Physics
Discussions

158   The nitrite produced in E2 is rapidly photolyzed at longer wavelengths (λ=290-390 nm)

159   (E3).

160

161 $NO_2^-(aq) + h\nu(+H^+, aq) \rightarrow NO(aq) + OH(aq)$,   E3

162

163   Nitrite can also react with OH or H^+ in the LLR to produce aqueous-phase NO_2 and

164   HONO [*Grannas et al.*, 2007]:

165

166    $NO_2^-(aq) + OH(aq) \rightarrow NO_2(aq) + OH^-(aq)$,   E4

167    $NO_2^-(aq) + H^+(aq) \rightarrow HONO(aq)$,   E5
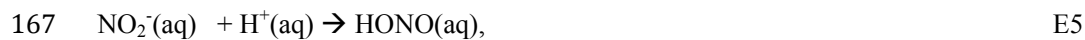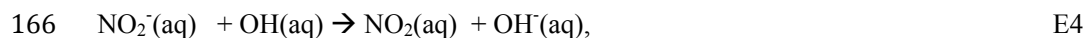
168

169   HONO can rapidly photolyze in the LLR to produce aqueous-phase NO and OH

170   [*Anastasio and Chu*, 2009]; due to its short lifetime the aqueous-phase OH remains in the

171   LLR, but the aqueous-phase NO can be transferred to the gas phase and ultimately be

172   released into the boundary layer. Aqueous-phase HONO can also be transferred to the gas

173   phase (HONO (aq) $\leftrightarrow$ HONO (g)) and released into the boundary layer, where it can

174   photolyze to produce gas-phase NO and OH [*Zhou et al.*, 2001].

175

176   Snow-sourced NO_x in the boundary layer can re-oxidize to HNO_3 via E6,

177

178    $NO_2(g) + OH(g) \rightarrow HNO_3(g)$,   E6

179

Atmospheric
Chemistry
and Physics
Discussions

Open Access

EGU

180   and redeposit to the snow surface within several days [*Levy and Moxim*, 1989, *Levine et*

181   *al.*, 1981], providing the snow with a recycled source of nitrate that is again available for

182   photolysis.

183

184   Nitrate nitrogen isotopes ($\delta^{15}N(NO_3^-)$) in the air and snow can provide useful information

185   about snow photochemistry, specifically, the degree of photolysis-driven recycling and

186   loss of nitrate from the snow. Nitrogen isotope ratios are expressed as $\delta^{15}N$, where $\delta =$

187   $R_{sample}/R_{reference} - 1$, $R = {}^{15}N/{}^{14}N$, and N_2-air is the reference material. Nitrate photolysis in

188   snow is a mass-dependent process and is associated with a large fractionation constant (ϵ)

189   of -47.9‰ at wavelengths shorter than 320 nm [*Berhanu et al.*, 2014a]. Nitrate photolysis

190   provides the boundary layer with a source of N_r that is highly depleted in ${}^{15}N$, leaving

191   highly enriched $\delta^{15}N(NO_3^-)$ deeper in the snow. Snow-sourced nitrate that is redeposited

192   to the snow surface is lighter than the remaining nitrate in the snow, leading to $\delta^{15}N(NO_3^-$

193   ) values that become more enriched with increasing depth within the snow photic zone.

194   $\delta^{15}N(NO_3^-)$ values in the atmosphere are also influenced by the relative importance of

195   different NO_x sources [see *Felix and Elliott,* 2014 for a summary]. For example, the

196   atmospheric $\delta^{15}N$ signature from anthropogenic NO_x sources, such as combustion of

197   fossil fuels, range from -19.0‰ to 25.0‰ [*Felix et al.,* 2012, *Walters et al.*, 2015]. The

198   $\delta^{15}N$ signature from soil microbial activity is generally lower than that of anthropogenic

199   activity and ranges from -50‰ to -20‰ [*Felix and Elliott*, 2014]. Observations of

200   atmospheric $\delta^{15}N(NO_3^-)$ in non-polluted, mid-latitude regions range from -6 to -2‰,

201   while $\delta^{15}N(NO_3^-)$ values measured in polluted regions range from 0 to 6‰ [*Morin et al.*,

202   2009].   In addition, atmospheric $\delta^{15}N(NO_3^-)$ is influenced by NO_x cycling [*Freyer et al.*,

Atmospheric
Chemistry
and Physics
Discussions

203   1993; *Walters et al*., 2016], NO_2 oxidation [*Walters and Michalski*, 2015], and the

204   partitioning of nitrate between its gas and particulate phases [*Heaton et al*., 1997].

205

206   In this study, we investigate the importance of snow photochemistry as a source of

207   reactive nitrogen oxides to the boundary layer in the Uintah Basin using chemical,

208   isotopic, and optical measurements from the snow collected during the UBWOS 2014

209   campaign. We use these observations of snow optical properties along with observations

210   of surface downwelling irradiance as inputs to a snow radiative transfer model to

211   calculate photolysis frequencies in the snow. The source of snow N_r is then calculated

212   simply by multiplying the calculated photolysis frequencies by the observed snow nitrate

213   concentrations. The calculated photolysis frequencies in snow are also used in a snow

214   photochemistry column model which is constrained by our observations of snow

215    $\delta^{15}N(NO_3^-)$. In Section 2 we describe the field, laboratory, and modeling techniques used

216   in this study. In Section 3 we present the chemical and optical measurements made

217   during UBWOS 2014 and model-calculated fluxes of snow-sourced N_r. In Section 4 we

218   estimate the contribution of snow-sourced N_r to the N_r burden in the Uintah Basin

219   boundary layer.

220

Atmospheric
Chemistry
and Physics
Discussions

Open Access

EGU

2. Methods

221

222

2.1. Field and Laboratory Observations

223

224

2.1.1. UBWOS 2014 Field Site Description and Meteorological Conditions

225

226 UBWOS 2014 occurred from January 17, 2014 to February 13, 2014 at the Horsepool

227 field-intensive site (40.1°N, 109.5°W) in the Uintah Basin, roughly 35 miles south of

228 Vernal, Utah. There are over 10,000 oil and natural gas wells in the basin connected by a

229 series of dirt roads. The meteorological conditions were relatively constant for most of

230 the campaign; wind speeds ranged from 1 to 3 m s^{-1} and often originated from the

231 southwest. Sky conditions were clear, temperatures ranged from 258 to 275 K, and

232 boundary layer heights generally ranged from 25 to 150 m. There were a few cloudy days

233 (January 29-February 4, February 10) during the campaign and the last several days

234 experienced temperatures above freezing. Daily maximum boundary layer O_3 mixing

235 ratios ranged from 45 ppb to 90 ppb, and the campaign-averaged daily-maximum

236 boundary layer O_3 mixing ratio was 61 ppb.

237

238 Snow covered the ground throughout the duration of the campaign, and ranged in depth

239 from 10 to 30 cm, depending on how snow was redistributed by wind after deposition.

240 The snow was deep enough to cover some of the lowest-lying vegetation, but branches

241 from bushes were still visible. Three snow events occurred before the campaign, one

242 event on December 4, which deposited most of the snow (19 cm), and two smaller events

243 on December 8 and December 19, which deposited roughly 3 cm and 1 cm of snow,

Atmospheric
Chemistry
and Physics
Discussions

Open Access

244   respectively. There was a distinct crust layer roughly 4 cm below the snow surface,

245   providing evidence of surface melting between the later two snowfall events. The

246   temperature difference between the soil and the air was at least 15 K for several weeks,

247   allowing vapor to redistribute through the snow, leading to the formation of large hoar

248   crystals (radiation equivalent mean ice grain radii [*Hansen and Travis*, 1974] (r_e) > 1200

249   μm) at all depths in the snow. There was one major snow event during the campaign on

250   January 30 through January 31 that deposited roughly 5 cm of fresh snow ($r_e \sim 100$ μm).

251   There were two smaller snow events on February 4 and February 10. On February 4 there

252   was no measureable snow accumulation and during the early-morning hours of February

253   10 there was 2 cm of fresh snow that subsequently melted several hours after sunrise.

254   Supplementary Figure 3B summarizes daily snow accumulation before and during the

255   campaign.

256

257   **2.1.2 Snowpit Measurements and Snow Sample Preparation**

258   Twelve snowpits were dug and measured approximately every 2 to 3 days during the

259   campaign. Snowpits were dug from the snow surface to about 1 cm above the subniveal

260   ground and ranged in depth from 9 to 24 cm. The snowpits were dug in a variety of

261   directions roughly 150 meters from the main Horsepool site, except for snowpit 5

262   (January 24), which was dug roughly 800 meters away from Horsepool. The snowpits

263   were dug wearing clean, nitrate-free gloves using a stainless steel spatula. For each

264   snowpit, vertical profiles (1-cm depth resolution) of snow density (ρ_{snow}), temperature,

265   and radiation equivalent ice grain radii (r_e) were measured using a Taylor-LaChapelle

266   snow density kit, a dial stem thermometer, and a laminated snow grid card with 1 mm

Atmospheric
Chemistry
and Physics
Discussions

267   grid spacing, respectively. Snow grains from each distinct snow layer were placed on the

268   snow grid card and a photograph was taken. The photographs were projected onto a

269   larger screen and the shortest dimension of each snow crystal was estimated. The shortest

270   dimension of a snow grain is the most optically important dimension [*Grenfell and*

271   *Warren*, 1999], and in this study, it is used to represent r_e. For hoar crystals, the smallest

272   dimension is the width of the crystal wall and for freshly-fallen crystals, the smallest

273   dimension is the radius of the rounded crystal. For each snowpit, approximately 1 kg of

274   snow was collected at 1-cm depth intervals and placed into 'whirl-pak' plastic bags. The

275   bags were kept covered while in the field and then immediately placed into a freezer once

276   back at the Utah State University (USU) Uintah Basin Campus in Vernal, Utah.

277   Supplementary section A shows detailed information on each snowpit.

278

279   **2.1.3. Optical Measurements**

280   The snow from each plastic bag was spooned into a clean glass beaker and melted in a

281   microwave oven at USU. The meltwater was transferred to a stainless steel funnel and

282   passed through a 0.4 μm Nuclepore filter, using an electric diaphragm vacuum pump to

283   create a partial vacuum in a volumetric flask. The Nuclepore filter collects insoluble light

284   absorbing impurities (LAI) in snow, including black carbon (BC) and non-black carbon

285   (non-BC) species, the latter of which encompass brown carbon, dust, and organics. The

286   volume of filtrate was measured, which ranged from 40 to 750 ml depending on impurity

287   content. After the Nuclepore filters dried overnight, the filters were frozen until further

288   analysis at the University of Washington (UW).

289

Atmospheric
Chemistry
and Physics
Discussions

Open Access

EGU

290   The absorption spectrum of each Nuclepore filter was measured using an ISSW

291   spectrophotometer [*Grenfell et al.*, 2011] in the Arctic Snow Laboratory at UW. The

292   Nuclepore filter is placed between two integrating spheres lined with Spectralon material

293   to create a fully diffuse medium. An Ocean Optics USB-650 spectrophotometer is used to

294   measure the absorption spectrum in units of optical depth, $\tau(\lambda)$ (dimensionless, e.g. cm^2

295   cm^{-2}), from λ=350-1000 nm in 10 nm intervals. A set of standard filters containing known

296   loadings of black carbon (Fullerene) is used to calibrate the ISSW spectrophotometer.

297   The spectral absorption measured by the spectrophotometer for each filter is

298   characterized by an Ångstrom exponent ($Å$), which represents the total absorption by both

299   BC and non-BC LAI on the filter between two visible wavelengths. $Å$ is calculated in E7:

300

301    $$Å(\lambda_1 \, to \, \lambda_2) = \frac{\ln\left(\frac{\tau(\lambda_1)}{\tau(\lambda_2)}\right)}{\ln\left(\frac{\lambda_2}{\lambda_1}\right)} \;,$$ E7

302

303   where λ_1=450 nm and λ_2=600 nm. The λ=450-600 nm range is chosen because the ISSW

304   spectrophotometer signal is most stable over this wavelength range. The total absorption

305   Ångstrom exponent on each filter along with assumed Ångstrom exponents for BC ($Å$=1)

306   and non-BC ($Å$=5) are used to estimate snow BC concentrations and the fraction of

307   ultraviolet (λ=300-350 nm) absorption by non-BC material (see *Doherty et al.*, 2010,

308   *Grenfell et al.*, 2011, *Zatko et al.*, 2013, and *Zatko and Warren*, 2015). Triplicate

309   measurements were performed for all samples.

310

311   Surface upwelling and downwelling irradiance was measured using a commercial

312   spectral   radiometer   equipped   with   a   photodiode   array   (Metcon   GMBH,

Atmospheric
Chemistry
and Physics
Discussions

313   http://www.metcon-us.com). Upwelling and downwelling UV-A and UV-B were

314   measured with Kipp and Zonen Model UV-S-AB-T radiometers. Radiometers were

315   placed at 2 m above ground (one up-facing and one down-facing) and were cleaned and

316   checked weekly to ensure that the radiometers remained directly perpendicular to the

317   ground. Detailed irradiance data is provided in the Supplemental Material.

318

319   **2.1.4. Chemical Concentration and Nitrate Isotopic Measurements**

320   In a laboratory on the USU campus in Vernal, UT, a 50 µl aliquot of snow meltwater that

321   was passed through the Nuclepore filter was used to measure ion (Cl$^-$, Br$^-$, NO$_3^-$, SO$_4^{2-}$,

322   Na$^+$, NH$_4^+$, K$^+$, Mg^{+2}, Ca^{+2}, oxalate) concentrations using a Metrohm 761 Compact Ion

323   Chromatograph Analyzer [*Quinn et al.*, 1998]. The nitrate in the remaining filtrate was

324   preconcentrated for isotopic analysis. Nitrate was preconcentrated by passing the

325   meltwater through an anion exchange resin (BioRad AG 1-X8) using an electric

326   diaphragm pump. The sample anions in the resin were eluted with 5x2 ml 1 M sodium

327   chloride (NaCl/Milli-Q water) solution into a 30 ml pre-cleaned sample bottle. This

328   method has been shown to ensure full recovery of nitrate [*Silva et al.*, 2000, *Frey et al.*,

329   2009] The solution was kept frozen in the dark until analysis in the University of

330   Washington IsoLab (http://isolab.ess.washington.edu/isolab/).

331

332   The denitrifier method [*Casciotti et al.*, 2002, *Kaiser et al.*, 2007, *Sigman et al.*, 2001]

333   was used to determine the nitrogen isotopic signature (δ^{15}N) in each snow sample.

334   Denitrifying bacteria, *Pseudomonas aureofaciens,* convert nitrate to nitrous oxide (N$_2$O)

335   gas in anaerobic conditions [*Casciotti et al.*, 2002, *Sigman et al.*, 2001] and N$_2$O is

Atmospheric
Chemistry
and Physics
Discussions

Open Access

EGU

336 transported via helium gas through a heated gold tube (800°C), where it thermally

337 decomposes into O_2 and N_2. After separation by gas chromatography, the O_2 and N_2 are

338 run through a Thermo Finnigan^{TM} DeltaPlus Advantage isotope ratio mass spectrometer

339 (IRMS), equipped with a Precon and GasBench II^{TM}. The $\delta^{15}N$ values were calculated

340 with respect to N_2 (air) via two international reference materials USGS32 ($\delta^{15}N = 180‰$)

341 and USGS34 ($\delta^{15}N = -1.8‰$), with IAEA ($\delta^{15}N = 4.7‰$) as a quality control standard. For

342 many samples, the $NaCl/NO_3^-$ solution was diluted with Milli-Q water to obtain the

343 optimal nitrate concentration (200 nmol in 2 ml) for each sample run on the IRMS.

344 Triplicate measurements were performed for all samples. The analytical uncertainty of

345 $\delta^{15}N(NO_3^-)$ (1σ) was 0.75‰ based on repeated measurements of the quality control

346 standard.

347

348 Aerosol nitrate was collected throughout the campaign in 12-hour intervals. Aerosol

349 nitrate was sampled from an inlet 13 meters above ground and drawn through a heated

350 (283K) pipe, where it was then collected on a two-stage, multi-jet cascade impactor. The

351 impactor tedlar films separates aerosols with diameters less than 2.5 μm from those with

352 diameters between 2.5 to 12.5μm. The aerosols were extracted from the filters and

353 analyzed using ion chromatography, following methods described in Quinn et al. [2000].

354 Gas-phase nitric acid was measured using an Acetate HR-ToF-CIMS instrument

355 throughout the campaign with 1-minute time resolution, as described in Yuan et al.

356 [2016].

357

358 **2.2. Calculations**

Atmospheric
Chemistry
and Physics
Discussions

359

2.2.1. Snow Radiative Transfer Model

A 4-stream, plane-parallel radiative transfer model using the discrete ordinates method with a δ-M transformation originally described in Grenfell et al. [1991] was used to calculate vertical profiles of UV actinic flux in each snowpit. This model properly treats layers with differing refractive indices and the 4-stream model produces albedo and absorptivity results that agree to within 1% of higher-order models representative of snow [*Wiscombe*, 1977], including DISORT [*Stamnes et al.*, 1988]. Vertical profiles of the ρ_{snow}, r_e, and LAI absorption are used to calculate vertical profiles of inherent optical properties (IOPs) in snow at the wavelengths relevant for photochemistry (UV). These wavelength-dependent IOPs include the bulk extinction coefficient in snow ($Kext_{tot}$) and the co-albedo of single scattering ($c\varpi_{eff}$); see Zatko et al. [2013] for more details about the IOP calculations. $Kext_{tot}$ and $c\varpi_{eff}$, along with observations of downwelling surface UV irradiance, solar zenith angle, cloud fraction, and soil albedo (0.1) [*Markvart et al.*, 2003, *Matthias et al.*, 2000] are used to calculate 1-cm resolution vertical profiles of UV actinic flux for each snowpit, following methods described in Zatko et al. [2013]. The UV actinic flux profiles are used to calculate depth-dependent photolysis rate constants for nitrate photolysis in snow as described below.

377

2.2.2. Snow-Sourced Reactive Nitrogen Flux Calculations

The modeled vertical profiles of actinic flux and observed snow nitrate concentrations are used to calculate daily-average fluxes of snow-sourced N_r from each snowpit according to E8.

382

383 $$F_{Nr}(z) = \int_{\lambda_0}^{\lambda_1} \sigma_{NO_3^-}(\lambda) \cdot \phi(T,pH) \cdot I(\lambda, z) \cdot [NO_3^-] \, d\lambda,$$ E8

384

385 $F_{Nr}(z)$ is the flux of snow-sourced N_r (molec cm^{-2} s^{-1}) at 1-cm depth (z) increments in the

386 snow, σ_{NO3}^- is the wavelength (λ)-dependent absorption cross-section for nitrate

387 photolysis (cm^2) from Berhanu et al. [2014], ϕ is the temperature- and pH-dependent

388 quantum yield for nitrate photolysis (ϕ, molec photon^{-1}) from Chu and Anastasio [2003]

389 (4.6×10^{-3} molec photon^{-1} at T=267 K), I is the depth (z)- and λ-dependent actinic flux in

390 the snow photic zone (photons cm^{-2} s^{-1} nm^{-1}), and $[NO_3^-]$ is the observed nitrate

391 concentration (ng g^{-1}) in each snow layer. E8 is integrated over the UV wavelength

392 region (λ=298-345 nm). The snow photic zone is defined as three times the e-folding

393 depth of UV actinic flux in snow [*Zatko et al.*, 2016]. The total flux of Nr to the boundary

394 layer, F_{Nr}, is calculated according to E9.

395

396 $$F_{Nr} = \sum_{z_0}^{z_{3e}} F_{Nr}(z)$$ E9

397

398 Observed surface downwelling irradiance values for a solar zenith angle of 65°, the

399 average SZA from mid-December to mid-February, are used for calculation of $I(\lambda,z)$ in

400 E8. Therefore the calculated F_{Nr} values represent daily-averaged F_{Nr} values. It is assumed

401 that all N_r escapes into the boundary layer due to its low solubility.

402

403 **2.2.3. Snow Photochemistry Column Model (TRANSITS)**

404 The flux of snow-sourced N_r from each snowpit is also calculated using a snow

405 photochemistry column model, TRansfer of Atmospheric Nitrate Stable Isotopes To the

406 Snow (TRANSITS) model [*Erbland et al.*, 2015]. TRANSITS is a multilayer, one-

407 dimensional model that simulates nitrate photochemistry in the snow and allows for

408 chemical exchange between the air and snow and calculates the isotopic composition of

409 snow nitrate. The model was originally developed to simulate snow nitrate photolysis and

410 subsequent nitrogen recycling at the air-snow interface on the East Antarctic plateau

411 (Dome C), and has been adapted to mid-latitude, shallow-snowpack conditions for this

412 study. The model has a well-mixed, atmospheric boundary layer with a height of 50 m

413 and a snow compartment containing up to 50 1-cm thick layers. In the atmosphere and in

414 each snow layer, the model solves a general mass-balance equation for nitrate

415 concentration and isotopic composition [*Erbland et al.*, 2015] at each time step (1 hour).

416

417 In TRANSITS, nitrate is deposited to the snow surface via dry deposition. Nitrate dry-

418 deposition is calculated using the campaign-averaged observed boundary layer mixing

419 ratios for HNO_3 (5784 ng m^{-3}) and NO_3^- (5777 ng m^{-3}) and an assumed dry-deposition

420 velocity of 0.03 cm s^{-1}, which is similar to the dry-deposition velocity used in Edwards et

421 al. [2013, 2014] (0.02 cm s^{-1}) (see Supplementary Table 1B for nitrate dry-deposition

422 fluxes). Nitrate diffuses through the snowpack based on a diffusion coefficient that is

423 dependent on temperature, pressure, snow specific surface area, snow density, and

424 tortuosity [*Crowley et al.*, 2010, *Durham et al.*, 1986, *Massmann*, 1998].

425

Atmospheric
Chemistry
and Physics
Discussions

426   We include only the major channel for the production of N_r from nitrate photolysis (E1)

427   in TRANSITS. The minor channels, E2-E5, all consist of chemistry of the intermediate in

428   nitrate photolysis, nitrite, which will photolyze or react rapidly once produced to form N_r.

429   We assume no export of snow-sourced N_r out of the atmospheric box, which is consistent

430   with the low wind speeds and stable boundary layer conditions observed during the

431   campaign. In this way there is no net loss of nitrate from the snow; however, vertical

432   redistribution of snow nitrate can occur which would result in distinctive vertical profiles

433   of nitrate concentration and $\delta^{15}N(NO_3^-)$ in the snow column. In addition to calculating the

434   flux of snow-sourced N_r, TRANSITS calculates vertical profiles of nitrate concentration

435   and isotopes ($\delta^{15}N(NO_3^-)$) in the snow. To calculate $\delta^{15}N(NO_3^-)$ in the snow, the nitrate

436   photolysis fractionation factor ($^{15}\varepsilon_{pho}$) is calculated at each time step and is dependent

437   upon the spectral distribution of the UV irradiance at the snow surface [*Bernhau et al.*,

438   2014, *Erbland et al.*, 2015]. Calculated $^{15}\varepsilon_{pho}$ values range from -88 to -35‰ between the

439   snowpits and are constant with snow depth.

440

441   In this study, TRANSITS is run at hourly resolution and is spun up beginning 27 days

442   before the start of the campaign using available atmospheric chemical (boundary layer

443   gas-phase and aerosol-phase nitrate) and meteorological data (air temperature and

444   pressure). A constant model boundary layer height of 50 m is assumed, which is a rough

445   estimate of daily-averaged boundary layer heights based on sodar facsimile data from

446   NOAA. The campaign-averaged observed boundary layer total nitrate (HNO_3+ NO_3^-)

447   mixing ratio (11,560 ng m^{-3}) was used to spin up the model. We collected and measured

448   atmospheric $\delta^{15}N(NO_3^-)$ throughout the campaign using a high volume air sampler with

Atmospheric
Chemistry
and Physics
Discussions

Open Access

EGU

449   Nylasorb filters. However, comparison with the nitrate ($HNO_3 + NO_3^-$) concentration

450   measurements from the PMEL two-stage, multi-jet cascade impactor measurements

451   revealed incomplete trapping. Since non-quantitative collection of nitrate may influence

452   the observed $\delta^{15}N(NO_3^-)$ values, the data was not used in this study. We instead use

453   surface snow $\delta^{15}N(NO_3^-)$ observations to represent atmospheric $\delta^{15}N(NO_3^-)$ (Figure 1a).

454   The TRANSITS snowpack is initialized by setting the snow height equal to 50 cm, the

455   snow photic zone to 6 cm (average photic zone depth for all snowpits), and using the

456   measured snow nitrate concentration and $\delta^{15}N(NO_3^-)$ vertical profiles from the first

457   snowpit of the campaign (January 15). The snowfall event on January 31 is simulated in

458   the model, but the other smaller events are not included. As the model evolves,

459   "snapshots" of the top 25-cm of snow are taken on days corresponding to each snowpit

460   and modeled profiles of nitrate concentration and $\delta^{15}N(NO_3^-)$ are compared to observed

461   profiles for each snowpit. Since vertical profiles of snow $\delta^{15}N(NO_3^-)$ are highly sensitive

462   to photochemical-driven redistribution of N_r in the snowpack [*Erbland et al.*, 2013,

463   2015], observed $\delta^{15}N(NO_3^-)$ provides a metric to assess model-calculated F_{Nr}.

464

465   **3. Results and Discussion**

466

467   **3.1. Observations**

468

469   **3.1. 1. Nitrate Concentrations and $\delta^{15}N(NO_3^-)$ in the Surface Snow**

470   Figure 1a shows mean surface snow $\delta^{15}N(NO_3^-)$ values for each snowpit, which range

471   from -5.5 to 11.1‰. The lowest observed surface snow $\delta^{15}N(NO_3^-)$ occurred immediately

472   after the only significant fresh snowfall event on Jan. 30 – 31 (-5.5‰). All other surface

473   snow samples were over 10‰ higher (5.2 to 11.1‰).

474

475   Figure 1b shows surface snow nitrate concentration measurements for each snowpit,

476   which range from 800 to 18,000 ng g^{-1}. Similar to $\delta^{15}N(NO_3^-)$, surface-snow nitrate

477   concentrations are lowest during the snowfall event on January 30 through January 31,

478   with the exception of February 11 when the snow was rapidly melting. Similarly,

479   boundary layer gas (HNO$_3$) and aerosol-phase (NO$_3^-$) nitrate mixing ratios decrease by a

480   factor of 6 between January 30 and January 31 (Supplementary Figure 1B) compared to

481   the rest of the field campaign.

482

483   Generally, the surface-snow $\delta^{15}N(NO_3^-)$ values fall within the range of primary

484   anthropogenic $\delta^{15}N$ values (4-25‰) [*Felix and Elliott*, 2014, *Walters et al.*, 2015].

485   During snow events the boundary layer is less stable, possibly allowing for the transport

486   of nitrate from remote sources outside the basin. In unpolluted, mid-latitude

487   environments, background atmospheric $\delta^{15}N(NO_3^-)$ ranges from -6 to -2‰ [*Morin et al.*,

488   2009]. During the major snowfall event on January 30 - 31, surface-snow $\delta^{15}N$ values are

489   ~10‰ lower compared to the rest of the campaign, suggesting that nitrate from beyond

490   the basin deposits to the snow surface.

491

Atmospheric
Chemistry
and Physics
Discussions

3.1.2. Snow Depth Profiles of Snow Optical Properties, Nitrate Concentrations, and
$\delta^{15}N(NO_3^-)$

492

493

494   In this section and the following sections, we focus on three snowpits (January 22,

495   January 31, February 4) as being representative of the time period before, during, and

496   after the largest snow event. The other 9 snowpits will not be discussed in detail, but

497   observed and modeled vertical profiles of chemical and optical measurements for all 12

498   snowpits can be found in Supplementary section A.

499

500   Figures 2a and 2b show vertical profiles of snow optical properties from an 18-cm deep

501   snowpit dug on January 22, which represents typical profiles from the beginning of the

502   field campaign until before the first snow event. Black carbon concentrations (C_{BC}, ng g^{-1})

503   range from 3 to 100 ng g^{-1} with the highest concentrations in the top several

504   centimeters of snow. Below 3 cm snow depth, C_{BC} decreases dramatically. Figure 2b

505   shows the average absorption Ångstrom exponent ($\AA$) from λ=450-600 nm. Over this

506   wavelength range, the dominant absorber at the snow surface is non-BC material ($\AA$ is

507   nearly 5), and both BC and non-BC contribute to absorption in sub-surface snow layers

508   ($\AA$ ranges from 2 to 2.7). Although BC and non-BC material are both responsible for the

509   absorption of radiation at λ=450-600 nm, non-BC material is responsible for between

510   99.6 and 100% of UV (λ=300-350 nm) absorption at all depths in this and in all snowpits

511   measured during the field campaign. The top 3 cm of snow contains the highest

512   concentration of both BC and non-BC material; we define this layer as the "dusty layer"

513   and this layer is represented as a brown shaded region in Figure 2.

514

515   Figures 2c and 2d show vertical profiles of snow optical properties from a 14-cm deep

516   snowpit dug on January 31. It snowed 5 cm between the afternoon of January 30 and

517   morning of January 31, and this new snow layer is evident in Figures 2c and 2d because

518   the dusty layer is now located roughly 5 cm below the snow surface. Figure 2c shows that

519   C_{BC} ranges from 5 to 100 ng g^{-1}; the maximum C_{BC} value has been buried deeper into the

520   snow. Figure 2d shows that $Å$ is close to 1 at the snow surface, indicating that BC

521   material dominates visible absorption at the snow surface immediately following the

522   fresh snowfall event. Figures 2e and 2f show vertical profiles of snow optical properties

523   from a 24-cm deep snowpit dug on February 4, 5 days after the snow event. In this

524   snowpit, C_{BC} ranges from 4 to 100 ng g^{-1} and $Å$ ranges from 1.7 to 3.4. Figures 2e and 2f

525   show that the original dusty layer is still located roughly 5 cm below the snow surface

526   and that a new dusty layer has formed at the snow surface.

527

528   Figure 3 shows observed vertical profiles of nitrate concentration and nitrogen isotopes

529   ($\delta^{15}N(NO_3^-)$) in snow from snowpits dug on January 22, January 31, and February 4.

530   Prior to the fresh snowfall event, snow nitrate concentrations are highest at the surface

531   (13,900 ng g^{-1}), and decrease exponentially in the top 10 cm to a low of 90 ng g^{-1} at 18

532   cm depth (Figure 3a). Immediately following the fresh snowfall event, the highest nitrate

533   concentrations (12,200 ng g^{-1}) are buried below 5 cm of fresh snow within the dusty layer

534   at 5 – 7 cm depth. The measured nitrate concentrations in the fresh snow layer range from

535   1,280 to 4,640 ng g^{-1}, which is up to 10 times lower than nitrate concentrations in the

536   dusty layer (Figure 3b). Five days after the fresh snowfall event, the highest nitrate

537   concentrations are still located roughly 7 cm below the snow surface within the dusty

Atmospheric
Chemistry
and Physics
Discussions

Open Access

EGU

538   layer, but surface nitrate concentrations are a factor of 2 higher compared to immediately

539   after the fresh snowfall event (Figure 3c).

540

541   Figure 3 shows measured snow $\delta^{15}N(NO_3^-)$ in each of the snowpits, which ranges from -

542   5.5‰ to 13‰. In the Jan. 22 snowpit, measured $\delta^{15}N(NO_3^-)$ is highest near the top and

543   bottom of the snowpit and lowest from 12-cm to 16-cm depth (Figure 3d). Following the

544   fresh snowfall event on Jan. 30 – 31, snow $\delta^{15}N(NO_3^-)$ values are lightest at the snow

545   surface and increase with depth in the fresh snow layer until the top of the dusty layer,

546   below which they decrease to -3.5‰ (Figure 3e). Five days after the fresh snowfall event,

547   measured $\delta^{15}N(NO_3^-)$ is most enriched in the dusty layer and at the snow surface (Figure

548   3f).

549

550   The last snowfall event prior to the start of the campaign occurred on December 19 and

551   resulted in roughly 1 cm of snow accumulation (Supplementary Figure 5A). The high

552   concentrations of LAI and nitrate in surface snow on January 22, combined with the

553   prolonged lack of snowfall, suggest continual dry-deposition of LAI to the surface snow.

554   We speculate that the major source of LAI originates from truck traffic on the dirt roads

555   in the area of the field site due to high values of $\mathring{A}$ (Figure 2). The factor of 150 and 17

556   decrease in nitrate and black carbon concentrations, respectively, from the surface to 18-

557   cm depth on January 22 suggests that minimal nitrate and LAI are transported (via e.g.,

558   diffusion or meltwater transport) from upper to lower snow layers. Immediately after the

559   snowfall event on January 31, nitrate and black carbon concentrations are 10 and 3 times

560   lower, respectively, in the surface snow layers compared to earlier in January, because

Atmospheric
Chemistry
and Physics
Discussions

561   the fresh snow has lower concentrations of these species. Even just five days after the

562   snowfall event on January 30 - 31, concentrations of nitrate and the Ångstrom exponent

563   ($\mathring{A}$) in the snow surface layer have increased by a factor of 2, likely due to dry deposition

564   of these species to the surface in the absence of snowfall.

565

566   The $\delta^{15}N(NO_3^-)$ profiles in snow do not immediately suggest significant photolysis-

567   driven redistribution of nitrate in the snowpack, which would result in the lightest values

568   at the surface, increasing exponentially with depth as observed in Antarctica [*Erbland et*

569   *al.*, 2013]. Prior to the first snowfall event on January 30-31, the surface dusty layer

570   contains the highest values of measured $\delta^{15}N(NO_3^-)$, which are similar to that expected

571   from primary emission of NO_x from anthropogenic sources [*Felix and Elliott*, 2014,

572   *Walters et al.*, 2015]. We speculate that the depleted $\delta^{15}N(NO_3^-)$ values towards the

573   bottom of the snowpit correspond to remote-sourced atmospheric nitrate that was

574   deposited during the large snow event (~20 cm of snow) on December 4. On January 31,

575   depleted $\delta^{15}N(NO_3^-)$ measurements at the snow surface suggest that there is deposition of

576   nitrate from less polluted regions surrounding the basin during the snow event. The

577   increase in surface snow $\delta^{15}N(NO_3^-)$ values after January 31 is likely due to deposition of

578   primary-sourced nitrate from anthropogenic NO_x sources in the basin. In the following

579   section, we examine the influence of photolysis of snow nitrate on the profiles of

580    $\delta^{15}N(NO_3^-)$ in snow.

581

582   **3.2. Calculations**

583

Atmospheric
Chemistry
and Physics
Discussions

584 3.2.1. Calculations of Snow Actinic Flux Profiles and Flux of Snow-Sourced N_r

585 Figure 4 shows calculated vertical profiles of UV actinic flux normalized to surface

586 downwelling irradiance for the three snowpits. The non-normalized actinic flux values

587 and surface downwelling irradiance values for all snowpits are presented in the

588 supplementary material. On January 22, the normalized actinic flux ratio is nearly 4 at the

589 snow surface because actinic flux is calculated by integrating irradiance over a sphere

590 (surface area of $4\pi r^2$) and also because scattering in snow dominates over absorption. In

591 Figure 4a, the actinic flux decreases to 2.9 within the top centimeter of snow due mainly

592 to UV absorption by non-BC in the surface snow layer. The actinic flux is rapidly

593 extinguished in the dusty layer and continues to decrease with increasing depth in the

594 snow, reaching a value of 0.01 at 18-cm depth. The blue shaded region represents the

595 snow photic zone (top 5 cm of snow) on January 22. The snow photic zones calculated in

596 this study (4-7 cm) are much shallower compared to calculated snow photic zones in

597 polar regions (72-207 cm in Antarctica, 6-51 cm in Greenland) [*Zatko et al.*, 2016]

598 because concentrations of LAI in the snow photic zone are at least five orders of

599 magnitude higher in Utah compared to Antarctica and Greenland.

600

601 In the snowpits following the fresh snowfall event, the existence of the dusty layer deeper

602 into the snow influences the vertical actinic flux profile and increases the photic zone

603 depth from 5 to 7 cm. The fresh snow at the surface contains less LAI compared to the

604 dusty layer, therefore actinic flux values are higher in the top several centimeters of snow

605 compared to actinic flux values measured before the snowfall event even though r_e values

606 in the new snow are a factor of 3.3-8.3 times smaller than the underlying depth hoar

Atmospheric
Chemistry
and Physics
Discussions

607   grains. Smaller r_e values lead to more scattering in the snow, which increases the

608   probability of absorption by LAI. Although actinic flux values are highest at the surface

609   on January 31, Figure 4b illustrates that UV radiation is rapidly attenuated below the

610   fresh snow layer because radiation is forward-scattered into the highly-absorbing dusty

611   layer. As a result, there is roughly an order of magnitude less actinic flux at 14-cm depth

612   on January 31 compared to January 22.

613

614   The presence of a new dusty layer on the snow surface five days after the fresh snowfall

615   event does not significantly alter the vertical profile of normalized UV actinic flux likely

616   because the LAI concentrations in surface layer are at least 5 times lower than LAI

617   concentrations in the original dusty layer (surface snow from January 22 snowpit).

618   Surface snow UV albedo is strongly influenced by the presence of LAI, and

619   Supplemental Figure 2B shows that snow UV albedo is lowest right before the snowfall

620   event on January 30-31 and highest immediately afterwards.

621

622   We use these actinic flux profiles (Figure 4) and the observed snow nitrate concentrations

623   (Figure 3a-c) to calculate daily-averaged $F_{Nr}(z)$ and F_{Nr} according to E8 and E9 for each

624   of the three snowpits. Prior to the fresh snowfall event, $F_{Nr}(z)$ decreases exponentially

625   with depth in the photic zone (Figure 5a). $F_{Nr}(z)$ is highest at the snow surface because

626   both actinic flux and snow nitrate concentrations are highest near the snow surface. Daily

627   average F_{Nr} summed over the snow photic zone is 5.6×10^8 molec cm^{-2} s^{-1} on January 22

628   (Figure 5a and Table 1).   Immediately following the fresh snowfall event, $F_{Nr}(z)$

629   decreases by a factor of 3 at the surface because of the factor of 4 decrease in surface

630   snow nitrate concentrations, which is partially compensated by the higher UV actinic flux

631   in the top of the snow photic zone (Figure 4b). The daily-averaged F_{Nr} on January 31 is

632   1.9×10^8 molec cm^{-2} s^{-1}, which is a factor of 3 lower than total F_{Nr} on January 22. Five

633   days later, $F_{Nr}(z)$ has increased by a factor of 2 at the surface due to the factor of 2

634   increase in surface nitrate concentrations (Figure 3c and 5c). The daily-averaged F_{Nr} on

635   February 4 is 3.2×10^8 molec cm^{-2} s^{-1}, which is a factor of 1.7 higher than total F_{Nr} on

636   January 31.

637

638   **3.2.2. Snow Photochemistry Column Model**

639   The snow chemistry column model is used to calculate the time-dependent flux of snow-

640   sourced N_r (F_{Nr}) and the depth profile of nitrate concentration and $\delta^{15}N(NO_3^-)$. Figure 6

641   shows the diurnal F_{Nr} values on January 22, January 31, and February 4. The daily-

642   averaged snow F_{Nr} on January 22 is 6.3×10^8 molec cm^{-2} s^{-1}. Immediately following the

643   snow event, the daily-averaged snow F_{Nr} decreases by a factor of 11 compared to January

644   22 (5.6×10^7 molec cm^{-2} s^{-1}). The dramatic difference in F_{Nr} is due to the differences in

645   nitrate concentrations in the top several centimeters of snow. Modeled snow nitrate

646   concentrations in the fresh snow layer on January 31 are between 30 and 300 times lower

647   compared to nitrate concentrations in the dusty layer. Five days after the snow event, the

648   daily-averaged snow F_{Nr} has increased by a factor of 2 (1.2×10^8 molec cm^{-2} s^{-1}) because

649   deposition of nitrate to the snow surface layer enhances surface nitrate concentrations and

650   thus F_{Nr}. Calculated daily average F_{Nr} using observed (section 3.2.1) and modeled

651   (TRANSITS) snow nitrate concentrations agree within a factor of ~2 (Table 1); modeled

Atmospheric
Chemistry
and Physics
Discussions

Open Access

652   F_{Nr} tends to be lower because modeled snow nitrate concentrations are lower than

653   observed (Figure 8).

654

655   Figure 7 shows hourly F_{Nr} values calculated for the entire UBWOS2014 campaign using

656   TRANSITS. From the start of the campaign until the fresh snow event on January 31, the

657   daily maximum F_{Nr} values increase as surface snow nitrate concentrations increase due to

658   continual dry-deposition of atmospheric nitrate to the snow surface. Immediately after the

659   snow event on January 31, daily maximum F_{Nr} values are lowered by more than a factor

660   of 10 due to decreased nitrate concentrations in the snow photic zone. Following the

661   snow event, the flux of snow-sourced N_r gradually increases again due to dry-deposition

662   of nitrate to the surface layer, although daily maximum F_{Nr} values remain lower

663   compared to values before the snow event throughout the remainder of the field

664   campaign.

665

666   Observed snow nitrate concentration and $\delta^{15}N(NO_3^-)$ values are used to assess results

667   from TRANSITS. $\delta^{15}N(NO_3^-)$ observations are particularly useful as a metric to assess

668   the F_{Nr} values calculated in TRANSITS because $\delta^{15}N(NO_3^-)$ vertical profiles are highly

669   sensitive to photolytic recycling and photolysis-driven loss of nitrate from snow. Figure

670   8 shows modeled snow nitrate concentrations and $\delta^{15}N(NO_3^-)$ from TRANSITS

671   compared to the observations. The general shapes of the modeled and measured vertical

672   profiles of nitrate concentration are in agreement for all three snowpits; both modeled and

673   measured nitrate concentrations are highest in the dusty layer and lowest near the bottom

674   of the snowpit (Figure 8a-c). Both the model and the observations show increased snow

Atmospheric
Chemistry
and Physics
Discussions

675   nitrate concentrations at the surface following the fresh snowfall event, but the model

676   tends to underestimate surface snow nitrate concentrations after the snow event.

677

678   Modeled $\delta^{15}N(NO_3^-)$ is also within the range of observations (Figure 8d-f). Modeled

679    $\delta^{15}N(NO_3^-)$ at the top surface snow layer becomes more depleted from the January 22 to

680   the January 31 snowpit reflecting the decrease in atmospheric $\delta^{15}N(NO_3^-)$ in the model

681   based on surface snow observations (Figure 1a). Without additional snowfall between

682   January 31 and February 4, surface snow $\delta^{15}N(NO_3^-)$ becomes more enriched in the

683   model over this time period because model atmospheric $\delta^{15}N(NO_3^-)$ becomes more

684   enriched (Figure 1a). In contrast, the observations retain this light $\delta^{15}N(NO_3^-)$ at a depth

685   of ~2 cm until the February 11 snowpit (see supplement A). The difference between

686   modeled and observed $\delta^{15}N(NO_3^-)$ at 2 cm depth after January 31 may be due to the

687   redistribution of surface snow by wind, and the fact that each snowpit was dug in a

688   slightly different location. Blowing snow will bury the surface snow with light

689    $\delta^{15}N(NO_3^-)$, and subsequent atmospheric deposition of more enriched $\delta^{15}N(NO_3^-)$ will

690   occur onto this new, wind-blown snow surface, retaining the light $\delta^{15}N(NO_3^-)$ at 2 cm

691   depth. In contrast to the observations, the model does not account for windblown

692   redistribution of snow, and calculates the time-evolution of nitrate concentration and

693    $\delta^{15}N(NO_3^-)$ gradients of a single snowpit.

694

695   As discussed in the introduction, laboratory-based quantum yield measurements range

696   from 0.003 to 0.6 [*Chu and Anastasio*, 2003, *Meusinger et al.*, 2014, *Zhu et al.*, 2010].

697   We use ϕ from Chu and Anastasio (4.6×10^{-3} at T=267 K, which is the average daytime

Atmospheric
Chemistry
and Physics
Discussions

Open Access

698   temperature during the campaign) in our base case simulation discussed above as it

699   results in calculated values of F_{Nr} in Antarctica and Greenland that are the same order of

700   magnitude as observations [*Zatko et al.*, 2016]. In a sensitivity study, we turn off

701   photolysis of snow nitrate in the model by setting $\phi = 0$. When snow nitrate photolysis is

702   turned off, snow nitrate concentrations change by less than 0.5% in all snowpits, resulting

703   in relatively little sensitivity of modeled snow nitrate concentration to snow

704   photochemistry because only this small fraction (< 0.5%) of nitrate is lost via photolysis

705   at all depths. Despite the large nitrogen isotope fractionation (ε = -88 to -35‰) resulting

706   from the photolysis of snow nitrate, the difference in modeled $\delta^{15}N(NO_3^-)$ when snow

707   nitrate is turned on ($\phi = 4.6 \times 10^{-3}$) and off ($\phi = 0$) is small because of the very small

708   fraction of nitrate photolyzed. When photolysis is turned on, snow $\delta^{15}N$ values are

709   slightly lower in the top several centimeters due to deposition of isotopically light, snow-

710   sourced nitrate and $\delta^{15}N$ values are slightly more enriched at depth. On January 22, the

711    $\delta^{15}N(NO_3^-)$ profiles in the snow photic zone with and without snow nitrate photolysis

712   differ by vary by $\leq 0.1‰$, on January 31 by $\leq 1.3‰$, and on February 4 by $\leq 0.3‰$.

713   Snow nitrate photolysis influences both the magnitude and gradient of the snow

714    $\delta^{15}N(NO_3^-)$ profiles on January 31 and February 4 more than January 22, likely because

715   light-absorbing concentrations are lower in the fresh snow layer.

716

717   In another sensitivity study, we calculate the maximum possible F_{Nr} in the Uintah Basin

718   by increasing the value of ϕ until modeled snow $\delta^{15}N(NO_3^-)$ falls outside the full range of

719   observations. Above $\phi = 0.2$, there is significant disagreement (when the maximum

720   change in $\delta^{15}N(NO_3^-)$ is $> 1\sigma$ of the mean $\delta^{15}N(NO_3^-)$ in all snowpits) between modeled

Atmospheric
Chemistry
and Physics
Discussions

721   and measured $\delta^{15}N(NO_3^-)$ values. Using $\phi = 0.2$ results in more enriched $\delta^{15}N(NO_3^-)$ at

722   depth due to enhanced photolytic loss, and more depleted $\delta^{15}N(NO_3^-)$ at the snow surface

723   due to the deposition of isotopically light snow-sourced nitrate. Using $\phi = 0.2$ results in a

724   maximum possible F_{Nr} at least 45 times larger than when using $\phi = 4.6\times10^{-3}$ for all

725   snowpits (see Table 1).

726

727

728   **4. Impact of Snow-Sourced N_r on the Boundary Layer Reactive Nitrogen Budget**

729

730   **4.1. NO_x**

731   We first assume that all N_r is NO_x and use F_{Nr} values calculated using the snow

732   photochemistry column model to estimate the impact of F_{NOx} on the reactive nitrogen

733   budget in the Uintah Basin. Using the best estimate for the quantum yield of nitrate

734   photolysis ($\phi=4.6\times10^{-3}$), the modeled daily-averaged flux of snow-sourced NO_x ranges

735   from 5.6×10^7 to 7.2×10^8 molec cm^{-2} s^{-1} and the maximum F_{Nr} value is 3.1×10^9 molec cm^{-2}

736   s^{-1} for the entire campaign (Supplementary Table 4B). The top-down NO_x emission

737   inventory for oil, gas, and all other sources excluding the Bonanza power plant in

738   Duchesne and Uintah counties is 6.5×10^6 kg NO_x yr^{-1} [*Ahmandov et al.*, 2015]. The

739   power plant is excluded because its smokestack emissions are above the boundary layer.

740   Assuming a constant NO_x emission rate and using the area of Duchesne (8433 km^2) and

741   Uintah counties (11658 km^2), the top-down NO_x emission estimate for the Uintah and

742   Duchesne counties is 1.2×10^{12} molec cm^{-2} s^{-1}. The emission of primary NO_x in these two

743   counties is thus at least 300 times higher than the estimated snow NO_x emissions,

Atmospheric
Chemistry
and Physics
Discussions

744   implying that snow-sourced NO_x fluxes likely do not influence the NO_x boundary layer

745   budget in the highly-polluted Uintah Basin. If the upper limit of $\phi = 0.2$ is used, snow-

746   sourced NO_x emissions are still at least 7 times smaller than primary NO_x emissions.

747   Although reactive nitrogen is likely being emitted from the snow into the boundary layer,

748   the snow-sourced NO_x signal is swamped by emissions from primary anthropogenic

749   sources in the Uintah Basin.

750

751   **4.2. HONO**

752   Only the major channel for snow nitrate photolysis (E1) is simulated in the TRANSITS

753   model, although nitrate can also photolyze via E2 and form both NO_x and HONO (E3-

754   E5). We estimate the maximum possible influence of snow-sourced N_r for boundary layer

755   HONO mixing ratios by assuming that all snow-sourced N_r is in the form of HONO. If

756   we assume that the campaign-maximum F_{Nr} value (3.1×10^9 molec cm^{-2} s^{-1}) is all HONO

757   that escapes from the snow into the boundary layer, a boundary layer height of 50 m, and

758   a lifetime of HONO of 18 minutes (at solar noon) [*Edwards et al.*, 2013], snow nitrate

759   photolysis would contribute a maximum of 25 pptv of HONO to the boundary layer at

760   solar noon. The modeled and observed Uintah Basin boundary layer HONO mixing ratios

761   presented in Edwards et al. [2014] range from ~20 pptv at night to up to 150 pptv during

762   the day, which suggests that the daytime fluxes of reactive nitrogen are not a significant

763   source of HONO to the boundary layer compared to other HONO sources in the basin.

764   Our estimated maximum HONO flux is comparable to snow-sourced HONO fluxes

765   measured at another polluted, mid-latitude location (Paris, France), estimates of which

766   ranged from $0.7-3.1 \times 10^{10}$ molec cm^{-2} s^{-1} (assuming a snow density of 0.36 g cm^{-3} and

Atmospheric
Chemistry
and Physics
Discussions

767   snow photic zone depth of 6 cm) [*Michoud et al.*, 2015]. If the upper limit of $\phi = 0.2$ is

768   used (campaign-maximum F_{Nr}=1.4x10^{11} molec cm^{-2} s^{-1}), the maximum boundary layer

769   HONO mixing ratio calculated using this approach is 1.1 ppbv at solar noon, which

770   would significantly impact boundary layer HONO mixing ratios in the Uintah Basin.

771   Given that HONO is thought to be only a minor fraction of total N_r emitted from snow

772   [*Beine et al.*, 2008], we consider this to be an overestimate.

773

774   **5. Conclusions**

775   This study estimates the influence of snow nitrate photolysis on the boundary layer

776   reactive nitrogen budget in the Uintah Basin, which is a region with heavy oil and natural

777   gas extraction processes. Observations of snow optical properties, including ultraviolet

778   (UV) light-absorbing impurities (e.g., black carbon, dust, organics), radiation equivalent

779   ice grain radii, and snow density from 12 snowpits measured during the Uintah Basin

780   Winter Ozone Study (UBWOS) 2014 are incorporated into a snowpack radiative transfer

781   model to calculate vertical profiles of UV actinic flux at 1-cm depth intervals in 12

782   snowpits dug during the campaign. The vertical UV actinic flux profiles along with

783   measurements of nitrate concentration are used to calculate snow-sourced reactive

784   nitrogen (N_r) fluxes associated with snow nitrate photolysis using both a simple equation

785   (E8) and a more complex snow photochemistry column model. Snow nitrate photolysis in

786   the column model is constrained by 1-cm depth resolved observations of $\delta^{15}N(NO_3^-)$ in

787   the snowpits, which is highly sensitive to UV photolysis [*Erbland et al.*, 2015].

788

789   Observations of UV light-absorbing impurities (LAI) reveal the highest concentrations in

790   the top several centimeters of all snowpits dug before the snowfall event on January 30

791   through January 31. This "dusty" layer experienced continual dry deposition for over a

792   month due to lack of snowfall, and UV radiation is rapidly attenuated in this snow layer.

793   Nitrate concentrations are up to a factor of 151 times higher in the surface, dusty layer

794   compared to other snow layers, suggesting that much of the nitrate in snow is also dry-

795   deposited to the snow surface. The LAI and nitrate concentrations in the 5 cm of fresh

796   snow that fell on January 30 through January 31 are a factor of 5 and 36 lower,

797   respectively, compared to dusty layer LAI and nitrate concentrations. The highest

798     $\delta^{15}N(NO_3^-)$ values in snow are generally located in the dusty layer, suggesting that much

799   of deposited nitrate is associated with primary NO_x emissions from anthropogenic

800   sources. Snow-surface $\delta^{15}N(NO_3^-)$ measurements range from -5.5‰ to 11.1‰ and

801   suggest that the local nitrate burden at Horsepool is dominated by primary emissions

802   from local anthropogenic sources, except during fresh snowfall, when nitrate formed

803   outside of the basin is an additional source of nitrate to the snow surface.

804

805   The snow-sourced N_r fluxes calculated using calculated UV actinic flux profiles and

806   observed snow nitrate concentrations are similar in magnitude to the daily-averaged

807   fluxes of snow-sourced N_r calculated using the more complex snow photochemistry

808   column model. The daily-averaged flux snow-sourced N_r (F_{Nr}) to the boundary layer

809   ranges from 5.6×10^7 to 7.2×10^8 molec cm^{-2} s^{-1} and the modeled campaign-maximum F_{Nr}

810   is 3.1×10^9 molec cm^{-2} s^{-1}. Snow-sourced NO_x fluxes are highly dependent on nitrate

811   concentrations in the top several centimeters of snow; F_{Nr} values are roughly an order of

812   magnitude higher in snowpits with a surface dusty layer compared to a buried dusty

813   layer. The top-down emission estimate of primary NO_x in the Uintah and Duchesne

814   counties reported in Ahmadov et al. [2015] is at least 300 times higher than estimated

815   snow NO_x emissions, assuming that all N_r is emitted as NO_x. This suggests that snow-

816   sourced NO_x fluxes likely have little influence on the boundary layer NO_x budget in the

817   highly-polluted Uintah Basin. Assuming that all N_r is emitted as HONO also suggests

818   that the snow-sourced reactive nitrogen fluxes associated with snow nitrate photolysis

819   also likely do not significantly contribute to boundary layer HONO mixing ratios in the

820   Uintah Basin. The relative importance of the flux of NO_x and HONO will influence the

821   impact of the recycling of reactive nitrogen in snow on the chemistry of the boundary

822   layer in snow-covered regions, but is unknown. Knowledge of the chemical speciation of

823   snow-source N_r is required for a better understanding of the full impact of snow on local

824   oxidant budgets. However, in the Uintah Basin, we conclude that air quality models can

825   safely neglect the recycling of reactive nitrogen in snow when identifying the most

826   effective strategies for reducing wintertime ozone abundances.

827

828   **Acknowledgements**

Atmospheric
Chemistry
and Physics
Discussions

844

845
846
847
848
849
850
851
852
853
854
855
856
857
858
859
860
861
862
863
864
865
866
867
868
869
870

Atmospheric
Chemistry
and Physics
Discussions

Open Access

References

Ahmadov, R., McKeen, S., Trainer, M., Banta, R., Brewer, A., Brown, S., Edwards, P.M., de Gouw, J.A., Frost, G.J., Gilman, J., Helmig, D., Johnson, B., Karion, A., Koss, A., Langford, A., Lerner, B., Olson, J., Oltmans, S., Peischl, J., Petron, G., Pichugina, Y., Roberts, J.M., Ryerson, T., Schnell, R., Senff, C., Sweeney, C., Thompson, C., Veres, P.R., Warneke, C., Wild, R., Williams, E.J., Yuan, B., Zamora, R.: Understanding high wintertime O3 pollution events in an oil- and natural gas-producing region of the western US. *Atmos. Chem. Phys.*, 15, 411-429, doi:10.5194/acp-15-411-2015, 2015.

Anastasio, C. and Chu, L.: Photochemistry of nitrous acid (HONO) and nitrous acidium ion (H_2ONO^+) in aqueous solution and ice. *Environ. Sci. Tech.*, 43, 1108-1114, 2009.

Beine, H., Colussi, A.J., Amoroso, A., Esposito, G., Montagnoli, M., Hoffman, M.R.: HONO emissions from snow. *Environ. Res. Lett.*, 3, 045005, 6, 2008.

Berhanu, T.A., Meusinger, C., Erbland, J., Jost, R., Bhattcharya, S. K., Johnson, M. S., Savarino, J.: Laboratory study of nitrate photolysis in Antarctic snow. II. Isotopic effects and wavelength dependence. J. Chem. Phys., 140, 244306, doi:10.1063/1.4882899, 2014.

Carter, W. P. L., Seinfeld. J.H.: Winter O3 formation and VOC incremental reactivities in the Upper Green River Basin of Wyoming. Atmos. Environ., 50, 255-266, doi:10.1016/j.atmosenv.2011.12.025, 2012.

Casciotti, K.L., Sigman, D.M., Hastings, M., Bohlke, J.K., Hilkert, A.: Measurement of the oxygen isotopic composition of nitrate in seawater and freshwater using the denitrifier method. *Anal. Chem.*, 74, 4905-4912, 2002.

Chu, L., and Anastasio. C.: Quantum Yields of Hydroxyl Radicals and Nitrogen Dioxide from the Photolysis of Nitrate on Ice. *J. Phys. Chem*., 107, 9594-9602, 2003.

Crowley, J.N., Ammann, M., Cox, R.A., Hynes, R.G., Jenkin, M.E., Mellouki, A., Rossi, M.J., Troe, J., Wallington, T.J.: Evaluated kinetic and photochemical data for atmospheric chemistry: Volume V – heterogeneous reactions on solid surfaces. Atmos. Chem. Phys., 10, 9059-9223, doi:10.5194/acp-10-9059-2010, 2010.

Delmas, R., Serca, D., Jambert, C.: Global inventory of NO_x sources. *Nutr. Cycl. Agroecosys.*, 48, 51-60, 1997.

Doherty, S. J., Warren, S. G., Grenfell, T. C., Clarke, A. D., and Brandt, R. E.: Light-absorbing impurities in Arctic snow. *Atmos. Chem. Phys.*, 10, 11647-11680, doi:10.5194/acp-10-11647-2010, 2010.

Domine, F., Bock, J., Voisin, D., Donaldson, D. J.: Can we model snow photochemistry? Problems with the current approaches. *J. Phys. Chem. A*, 117, 4733-4749, doi: 10.1021/jp3123314 2013.

917   Durham, J.L., Stockburger, L.: Nitric acid-air diffusion coefficient: Experimental
918   determination. *Atmos. Environ.*, 20(3), 559-563, 1986.
919
920   Edwards, P.M., Young, C.J., Aikin, K., de Gouw, J., Dube, W., Geiger, P., Gilman, J.,
921   Helmig, D., Holloway, J.S., Kercher, J., Lerner, B., Martin, R., McLaren, R., Parrish,
922   D.D., Peischl, J., Roberts, J.M., Ryerson, T.N., Thornton, J., Warneke, C., Williams, E.J.,
923   Brown, S.S.: O3 photochemistry in an oil and natural gas extraction region during winter:
924   simulations of a snow-free season in the Uintah Basin, Utah. *Atmos. Chem. Phys.*, 13,
925   8955-8971, doi:10.5194/acp-13-8955-2013, 2013.
926
927   Edwards, P.M., Brown, S., Roberts, J., Ahmadov, R., Banta, R., de Gouw, J., Dube, W.,
928   Field, R., Flynn, J., Gilman, J., Graus, M., Helmig, D., Koss, A., Langford, A., Lefer, B.,
929   Lerner, B., Li, R., Li, S., McKeen, S., Murphy, S., Parrish, D., Senff, C., Soltis, J., Stutz,
930   J., Sweeney, C., Thompson, C., Trainer, M., Tsai, C., Veres, P., Washenfelder, R.,
931   Warneke, C., Wild, R., Young, C., Yuan, B., Zamora, R.: High O3 pollution from
932   carbonyl photolysis in an oil and gas basin. *Nature*, 514, 351-354,
933   doi:10.1038/nature13767, 2014.
934
935   Erbland, J., Savarino, J., Morin, S., France, J.L., Frey, M.M., King, M.D.: Air-snow
936   transfer of nitrate on the East Antarctic plateau – Part 2: An isotopic model for the
937   interpretation of deep ice-core records. *Atmos. Chem. Phys.*, 15, 12079-12113,
938   doi:10.5194/acpd-15-12079-2015, 2015.
939
940   Felix, J.D., Elliott, E.M., Shaw, S.L: Nitrogen isotopic composition of coal-fired power
941   plant NO_x: Influence of emissions controls and implications for global emission
942   inventories. *Env. Sci. Tech.*, 46, 3528-3535, 2012.
943
944   Felix, J.D., Elliot, E.M.: Isotopic composition of passively collected nitrogen dioxide
945   emissions: Vehicle, soil and livestock source signatures. *Atmos. Environ.*, 92, 359-366,
946   doi:10.1016/j.atmosenv.2014.04.005, 2014.
947
948   Field, R.A., Soltis, J., McCarthy, M.C., Murphy, S., Montague, D.C.: Influence of oil and
949   gas field operations on spatial and temporal distributions of atmospheric non-methane
950   hydrocarbons and their effect on O3 formation in winter. *Atmos. Chem. Phys.*, 15, 3527-
951   3542, doi:10.5194/acp-15-3527-2015, 2015.
952
953   Frey, M. M., Savarino, J., Morin, S., Erbland, J., and Martins, J. M. F.: Photolysis imprint
954   in the nitrate stable isotope signal in snow and atmosphere of East Antarctica and
955   implications for reactive nitrogen cycling. *Atmos. Chem. Phys.*, 9, 8681-8696, 2009.
956
957   Freyer, H.D., Kley, D., Volz-Thomas, A., Kobel, K.: On the interaction of isotopic
958   exchange processes with photochemical reactions in atmospheric oxides of nitrogen. *J.
959   Geophys. Res.*, 98, D8, 14791-14786, doi: 10.1029/93JD00874, 1993.
960

Atmospheric
Chemistry
and Physics
Discussions

961   Gilman, J.B., Lerner, B.M., Kuster, W.C., de Gouw, J.A.: Source signature of volatile
962   organic compounds from oil and natural gas operations in northeastern Colorado.
963   *Environ. Sci. Technol.*, 47, 1297-1305, doi:10.1021/es304119a, 2013.

964

965   Grannas, A. M., Jones, A. E., Dibb, J., Ammann, M., Anastasio, C., Beine, H. J., Bergin,
966   M., Bottenheim, J., Boxe, C. S., Carver, G., Chen, G., Crawford, J. H., Domine, F., Frey,
967   M. M., Guzman, M. I., Heard, D. E., Helmig, D., Hoffman, M. R., Honrath, R. E., Huey,
968   L. G., Hutterli, M., Jacobi, H. W., Klan, P., Lefer, B., McConnell, J., Plane, J., Sander,
969   R., Savarino, J., Shepson, P. B., Simpson, W. R., Sodeau, J. R., von Glasow, R., Weller,
970   R., Wolff, E. W., Zhu, T.: An overview of snow photochemistry: evidence, mechanisms
971   and impacts. *Atmos. Chem. Phys.*, 7, 4329-4373, 2007.

972

973   Grenfell, T. C.: A Radiative Transfer Model for Sea Ice With Vertical Structure
974   Variations. *J. Geophys. Res.*, 96, 16991-17001, 1991.

975

976   Grenfell, T.C., Warren, S.G.: Representation of a nonspherical ice particle by a collection
977   of independent spheres for scattering and absorption of radiation. *J. Geophys. Res.*,
978   104(D24), 31697-31709, 1999.

979

980   Grenfell, T.C., Doherty, S.J., Clarke, A.D., Warren, S.G.: Light absorption from
981   particulate impurities in snow and ice determined by spectrophotometric analysis of
982   filters. Appl. Opt., 50(8), 2037-2048, doi:10.1364/AO.50.002037, 2011.

983

984   Guenther, A., Hewitt, N.C., Erickson, D., Fall, R., Geron, C., Graedel, T., Harley, P.,
985   Klinger, L., Lerdau, M., McKay, W.A., Pierce, T., Scholes, B., Steinbrecher, R.,
986   Tallamraju, R., Taylor, J., Zimmerman, P.: A global model of natural volatile organic
987   compound emissions. *J. Geophys. Res.*, 100(D5), 8873-8892, 1995.

988

989   Hansen, J.E., Travis, L.D.: Light scattering in planetary atmospheres. *Space. Sci. Rev.*,
990   16, 527-610, 1974.

991

992   Heaton, T. H. E., Spiro, B., Robertson, M.C., *Oecologia*, 109, 4, 600-607, 1997.

993

994   Helmig, D., Thompson, C.R., Evans, J., Boylan, P., Hueber, J., Park, J.H.: Highly
995   elevated atmospheric levels of volatile organic compounds in the Uintah Basin, Utah.
996   *Environ. Sci. Technol.*, 48, 4707-4715, doi:10.1021/es405046r, 2014.

997

998   Honrath, R.E., Guo, S., Peterson, M.C., Dziobak, M.P., Dibb, J.E., Arsenault, M.A.:
999   Photochemical production of gas phase NO_x from ice crystal NO_3^-. *J. Geophys. Res.*,
1000   105(D19), 24183-24190, 2000.

1001

1002   Kaiser, J., Hastings, M.G., Houlton, B.Z., Rockmann, T., Sigman, D.M.: Triple oxygen
1003   isotope analysis of nitrate using the denitrifier method and thermal decomposition of
1004 N_2O. *Anal. Chem.*, 79, 599-607, doi:10.1021/ac061022s, 2007.
1005

Atmospheric
Chemistry
and Physics
Discussions

1006 Levine, J.S., Rogowski, R.S., Gregory, G.L., Howell, W.E., Fishman, J.: Simultaneous
1007 measurements of NOx, NO, and O3 production in a laboratory discharge: atmospheric
1008 implications. *Geophys. Res. Lett.*, 8, 357-360, 1981.

1010 Levy, H., Moxim, W.J.: Simulated global distribution and deposition of reactive nitrogen
1011 emitted by fossil fuel combustion. *Tellus*, 41B, 256-271, 1989.

1013 Logan, J.A., Nitrogen oxides in the troposphere: Global and regional budgets. *J.*
1014 *Geophys. Res.*, 88(C15), 10785-10807, doi:10.1029/JC088iC15p10785, 1983.

1016 Mack, J., and Bolton, J. R.: Photochemistry of nitrite and nitrate in aqueous solution: A
1017 review. *J. Photochem. Photobiol.* A., 128, 1-13, 1999.

1019 Martin, R., Moore, K., Mansfield, M., Hill, S., Harper, K., Shorthill, H.: Final report:
1020 Uintah Basin winter O3 and air quality study, December 2010 – March 2011. Energy
1021 Dynamics Laboratory, document number: EDL/11-039, 2011.

1023 Massman, W.J. A review of the molecular diffusivities of H_2O, CO_2, CH_3, CO, O_3, SO_2,
1024 NH_3, N_2O, NO, and NO_2 in air, O_2 and N_2 near STP. *Atmos. Environ.*, 32(6), 1111-1127,
1025 doi:10.1016/S1352-230(97)00391-9, 1998.

1027 Markvart, T., Castalzer, L.: Practical handbook of photovoltaics: fundamentals and
1028 applications. Elsevier. ISBN 1-85617-390-9, 2003.

1030 Matthias, A.D., Fimbres, A., Sano, E.E., Post, D.F., Accioly, L., Batchily, A.K., Ferreira,
1031 L.G.: Surface roughness effects on soil albedo. *Soil Sci. Soc. Am.* J., 64, 1035-1041,
1032 2000.

1034 Meusinger, C., Berhanu, T.A., Erbland, J., Savarino, J., Johnson, M.S.: Laboratory study
1035 of nitrate photolysis in Antarctic snow. I. Observed quantum yield, domain of photolysis,
1036 and secondary chemistry. *J. Chem. Phys.*, 140, 244305, doi:10.1063/1.4882898, 2014.

1038 Michoud, V., Doussin, Jean-Francois, Colomb, A., Afif, C., Borbon, A., Camredon, M.,
1039 Aumont, B., Legrand, M., Beekman, M.: Strong HONO formation in a suburban site
1040 during snowy days. *Atmos. Environ.*, 116, 155-158, doi:10.1016/j.atmosenv.2015.06.040,
1041 2015.

1043 Morin, S., Savarino, J., Frey, M.M., Domine, F., Jacobi, H.-W., Kaleschke, L., Martins,
1044 J.M.F.: Comprehensive isotopic composition of atmospheric nitrate in the Atlantic Ocean
1045 boundary layer from 65°S to 79°N. *J. Geophys. Res.*, 114, D05303,
1046 doi:10.1029/208JD010696, 2009.

1048 Oltmans, S.J., Schnell, R.C., Johnson, B.J., Petron, G., Mefford, T., Neely III, R.:
1049 Anatomy of wintertime O3 production associated with oil and gas extraction activity in
1050 Wyoming and Utah. *Elem. Sci. Anth.*, 2, 000024, doi:10.12952/journal.elementa.000024,
1051 2014a.

Atmospheric
Chemistry
and Physics
Discussions

1052
1053 Quinn, P.K., Coffman, D.J., Kapustin, V.N., Bates, T.S., Covert, D.S.: Aerosol optical
1054 properties in the MBL during ACE-1 and the underlying chemical and physical aerosol
1055 properties. J. Geophys. Res., 103, 16547-16564, 1998.
1056
1057 Quinn, P.K., Bates, T.S., Miller, T.L., Coffman, D.J., Johnson, J.E., Harris, J.M., Ogren,
1058 A., Forbes, G., Anderson, T.L., Covert, D.S., Rood, M.J.: Surface submicron aerosol
1059 chemical composition: what fraction is not sulfate? *J. Geophys. Res*., 105(D5), 6785-
1060 6805, doi:10.1029/1999JD901034, 2000.
1061
1062 Rappengluck, B., Ackermann, L., Alvarez, S., Golovko, J., Buhr, M., Field, R.A., Soltis,
1063 J., Montague, D.C., Hauze, B., Adamson, S., Risch, D., Wilkerson, G., Bush, D.,
1064 Stoekenius, T., Keslar, C.: Strong wintertime O3 events in the Upper Green River basin,
1065 Wyoming. *Atmos. Chem. Phys*., 14, 4909-4934, doi.10.5194/acp-14-4909-2014, 2014.
1066
1067 Schnell, R.C., Oltmans, S.J., Neely, R.R., Endres, M.S., Molenar, J.V., White, A.B.:
1068 Rapid photochemical production of O3 at high concentrations in a rural site during
1069 winter. *Nat. Geosci*., 2, 120-122, doi:10.1038/ngeo415, 2009.
1070
1071 Sigman, D.M., Casciotti, K.L., Andreani, M., Barford, C., Galanter, M., Bohlke, J.K.: A
1072 bacterial method for the nitrogen isotopic analysis of nitrate in seawater and freshwater.
1073 *Anal. Chem*., 73, 4145-4153, doi:10.1021/ac010088e, 2001.
1074
1075 Silva, S.R., Kendall, C., Wilkinson, D.H., Ziegler, A.C., Chang, C.C.Y., Avanzino, R.J.:
1076 A new method for collection of nitrate from fresh water and analysis of the nitrogen and
1077 oxygen isotope ratios. *J. Hydrol*., 228, 22-36, 2000.
1078
1079 Stamnes, K., Tsay, S., Wiscombe, W., Jayaweera, K.: Numerically stable algorithm for
1080 discrete-ordinate-method radiative transfer in multiple scattering and emitting layered
1081 media. *Appl. Opt*., 27, 2502-2509, 1988.
1082
1083 Thompson, A.M., The oxidizing capacity of the Earth's atmosphere: Probable past and
1084 future changes. *Science*, 256, 1157-1165, 1992.
1085
1086 US EIA (US Energy Information Administration): Annual energy outlook 2014 Early
1087 Release Overview, Office of Integrated and International Energy Analysis US
1088 Department of Energy, Washington, DC 20585, available at:
1089 http://www.eia.gov/forecasts/aeo/er/pdf/0383er(2014).pdf (last access 24 March 2015),
1090 Report, 2014.
1091
1092 Warneke, C., Geiger, F., Edwards, P.M., Dube, W., Petron, G., Kofler, J., Zahn, A.,
1093 Brown, S.S., Graus, M., Gilman, J.B., Lerner, B.M., Peischl, J., Ryerson, T.B., de Gouw,
1094 J.A., Roberts, J.M.: Volatile organic compound emissions from the oil and natural gas
1095 industry in the Uintah Basin, Utah: oil and gas well pad emissions compared to ambient
1096 air composition. *Atmos. Chem. Phys*., 14, 10977-10988, doi:10.5194/acp-14-10977-2014,
1097 2014.

Atmospheric
Chemistry
and Physics
Discussions

1098
1099   Warren, S.G., Brandt, R.E., Grenfell, T.C.: Visible and near-ultraviolet absorption
1100   spectrum of ice from transmission of solar radiation into snow. *Appl. Opt*., 45, 21, 2006.
1101
1102   Walters, W.W., Goodwin, S.R., Michalski, G.: Nitrogen stable isotope composition $\delta^{15}N$
1103   of vehicle-emitted NO_x. *Environ. Sci. Tech*., 49, 2278-2285, doi:10.1021/es505580v,
1104   2015.
1105
1106   Walters, W.W., Michalski, G.:Theoretical calculation of nitrogen isotope equilibrium
1107   exchange fractionation factors for various NO_y molecules. *Geochem. Cosmochem. Acta*.,
1108   164, 284-297, doi:10.1016/j.gca.2015.05.029, 2015.
1109
1110   Walters, W.W., Simonini, D.S., Michalski, G.: Nitrogen isotope exchange between NO
1111   and NO_2 and its implications for $\delta^{15}N$ variations in tropospheric NO_x and atmospheric
1112   nitrate. *Geophys. Res. Lett*., 43, 1, 440-448, 10.1002/2015Gl066438, 2016.
1113
1114   Wiscombe, W.J.: The delta-M method: Rapid yet accurate radiative flux calculations for
1115   strongly asymmetric phase functions. *J. Atmos. Sci*., 34, 1408-1422, 1977.
1116   Yuan, B., Liggio, J., Wentzell, J., Li, S. M., Stark, H., Roberts, J. M., Gilman, J., Lerner,
1117   B., Warneke, C., Li, R., Leithead, A., Osthoff, H. D., Wild, R., Brown, S. S., and de
1118   Gouw, J. A.: Secondary formation of nitrated phenols: insights from observations during
1119   the Uintah Basin Winter Ozone Study (UBWOS) 2014, *Atmos. Chem. Phys*., 16, 2139-
1120   2153, 10.5194/acpd-16-2139-2016, 2016.
1121
1122   Zatko, M.C., Grenfell, T.C., Alexander, B., Doherty, S.J., Thomas, J.L., Yang, X., The
1123   influence of snow grain size and impurities on the vertical profiles of actinic flux and
1124   associated NO_x emissions on the Antarctic and Greenland ice sheets. *Atmos*. *Chem*.
1125   *Phys*., 13, 3547-3567, doi:10.5194/acp-13-3547-2013, 2013.
1126
1127   Zatko, M.C. and Warren, S.G.: East Antarctic sea ice in spring: spectral albedo of snow,
1128   nilas, frost flowers, and slush; and light-absorbing impurities in snow. *Ann. Glaciol*.
1129   *Special Issue: Sea ice in a changing environment,* 56(69), doi:10.3189/2015AoG69A574,
1130   2015.
1131
1132   Zatko, M.C., Geng, L., Alexander, B., Sofen, E., Klein, K.: The impact of snow nitrate
1133   photolysis on boundary layer chemistry and the recycling and redistribution of reactive
1134   nitrogen across Antarctica and Greenland in a global chemical transport model. *Atmos*.
1135   *Chem. Phys*., 16, 2819-2842, doi:10.5194/acp-16-2819-2016, 2016.
1136
1137   Zhou, X., Beine, H.J., Honrath, R.E., Fuentes, J.D., Simpson, W., Shepson, P.B.,
1138   Bottenheim, J.W.: Snowpack photochemical production of HONO: a major source of OH
1139   in the Arctic boundary layer in springtime. *Geophys. Res. Lett*., 28(21), 4087-4090, 2001.
1140
1141   Zhu, C., Xiang, B., Chu, L.T., Zhu, L.: 308 nm Photolysis of Nitric Acid in the Gas
1142   Phase, on Aluminum Surfaces, and on Ice Films. *J. Phys. Chem. A*., 114, 2561-2568, doi:
1143   10.1021/jp909867a, 2010.

Atmospheric
Chemistry
and Physics
Discussions

1144   Table 1. Snow photic zone depth and daily-averaged modeled F_{Nr} calculated using E8
1145   and the TRANSITS model on January 22, January 31, and February 4.

Pit Date	Photic zone depth (cm)	Daily-averaged F_{Nr} (molec cm^{-2} s^{-1})		
		E8	TRANSITS ($\phi = 4.6 \times 10^{-3}$)	TRANSITS ($\phi = 0.2$)
January 22	5.0	5.6×10^8	6.3×10^8	2.9×10^{10}
January 31	7.0	1.9×10^8	5.6×10^7	2.7×10^9
February 4	7.0	3.2×10^8	1.2×10^8	5.6×10^9

1146
1147
1148
1149
1150
1151
1152
1153
1154
1155
1156
1157
1158
1159
1160
1161
1162
1163
1164
1165
1166
1167

Atmospheric
Chemistry
and Physics
Discussions

Open Access

EGU
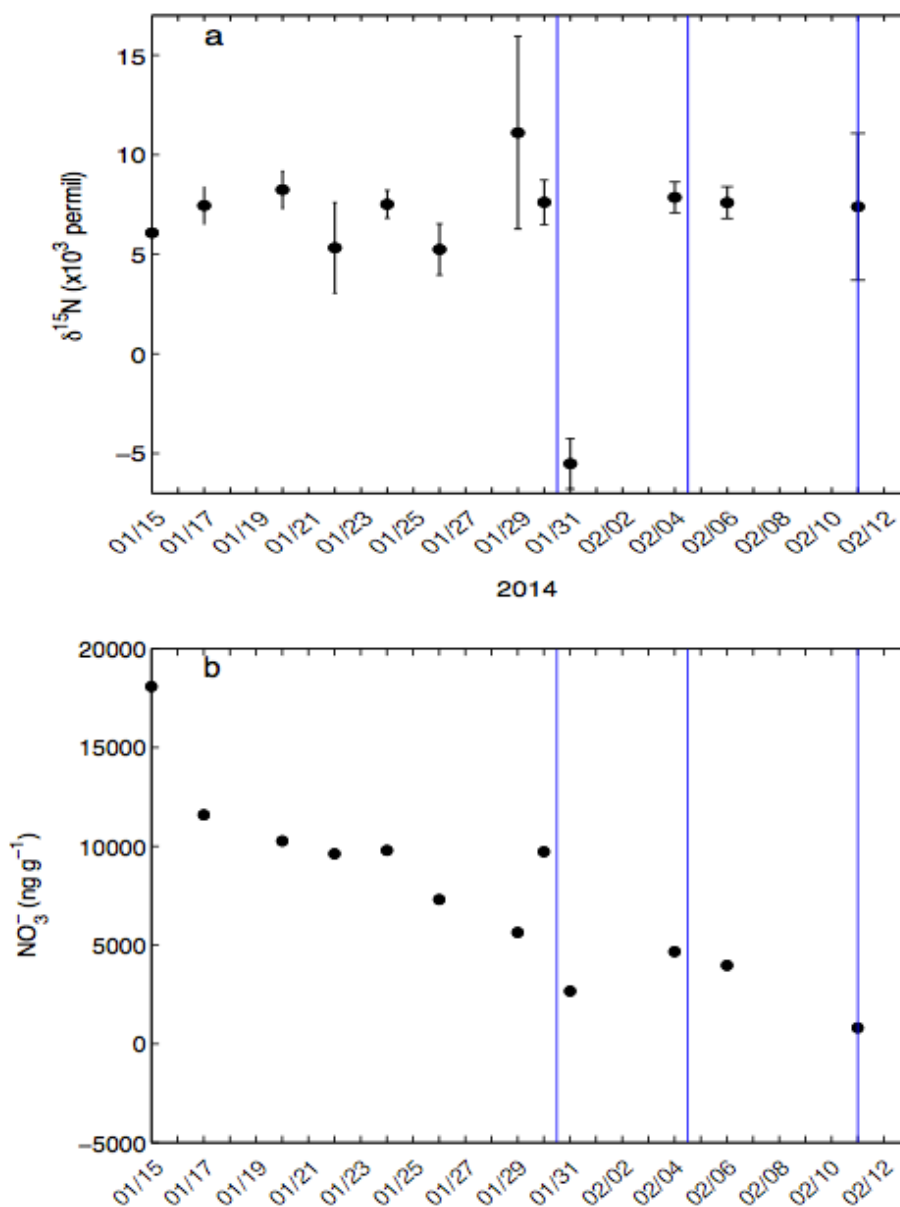
1168
1169
1170   Figure 1. (a) Mean surface snow (top 1 cm) $\delta^{15}N(NO_3^-)$ observations (‰) for triplicate
1171   measurements from each snowpit (close circles). The full range of triplicate measured
1172   surface snow $\delta^{15}N(NO_3^-)$ for each snowpit is also indicated (vertical black lines). (b)
1173   Surface snow nitrate concentration measurements (ng g^{-1}) for each snowpit. The
1174   uncertainty in the concentration measurements is 0.75‰. The vertical blue lines indicate
1175   snowfall events.
1176

Atmospheric
Chemistry
and Physics
Discussions

1177

1178
1179 Figure 2. Snow optical properties measured on January 22 (top), January 31 (middle), and
1180 February 4 (bottom). (top) Vertical profiles of mean snow black carbon (C_{BC}, ng g^{-1})
1181 measurements and the full range of C_{BC} measured at each depth (horizontal black lines),
1182 (bottom) mean Ångstrom exponent (Å, unitless) measurements and the full range of Å
1183 measured at each depth (horizontal black lines). The brown shaded region represents the
1184 dusty layer as defined in the text.
1185
1186
1187
1188
1189
1190
1191
1192
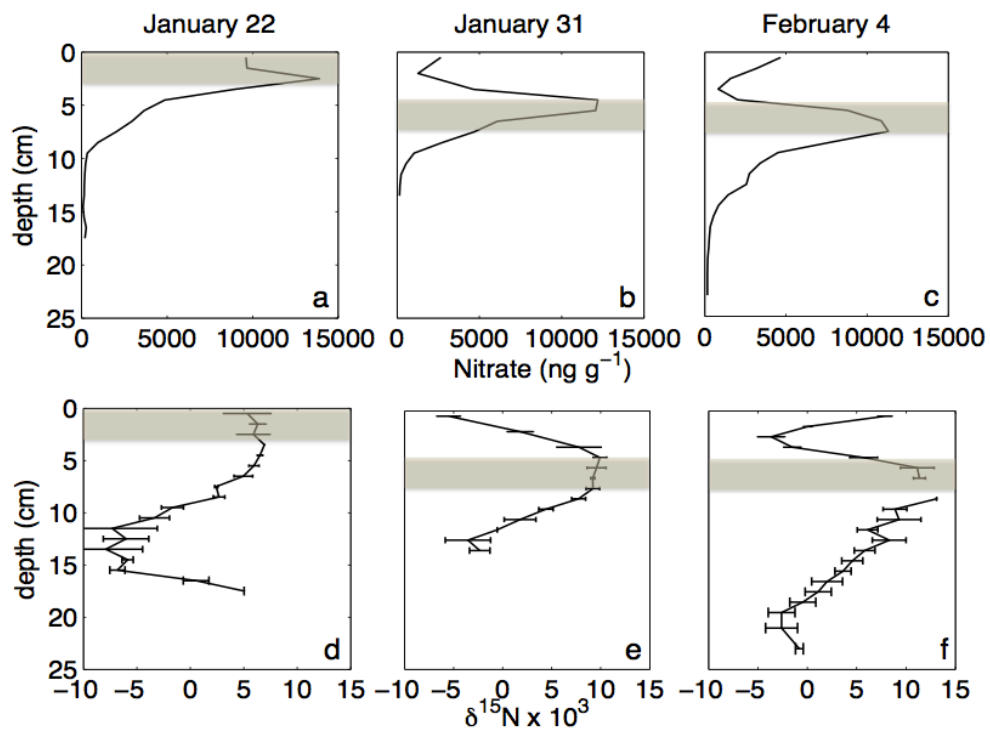
Figure 3. Observed vertical profiles of nitrate concentration (top) and its nitrogen isotopes (bottom) in snow on January 22 (left), January 31 (center), and February 4 (right). The brown shaded region represents the dusty layer.

Atmospheric
Chemistry
and Physics
Discussions

Open Access

EGU
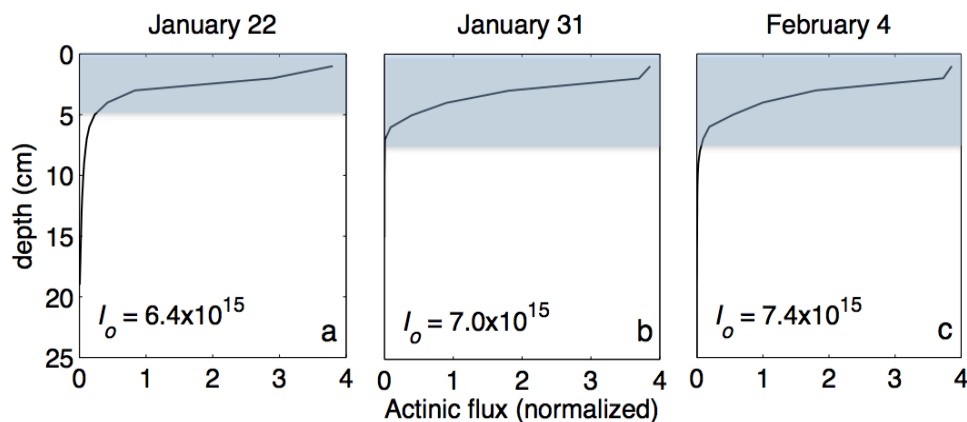
1204
1205 Figure 4. Modeled vertical profiles of UV actinic flux (I, photons cm^{-2} s^{-1}) normalized to
1206 surface downwelling irradiance (I_o, photons cm^{-2} s^{-1}). Also presented is measured total
1207 UV I_o (λ=300-350 nm) for a solar zenith angle of 60° on each day. The blue shaded
1208 region represents the snow photic zone.
1209
1210
1211
1212
1213
1214
1215
1216
1217
1218
1219
1220
1221
1222

1223

January 22 January 31 February 4

$F_{Nr} = 5.6 \times 10^8$ a

$F_{Nr} = 1.9 \times 10^8$ b

$F_{Nr} = 3.2 \times 10^8$ c

depth (cm)

$F_{Nr}(z)$ $\times 10^8$
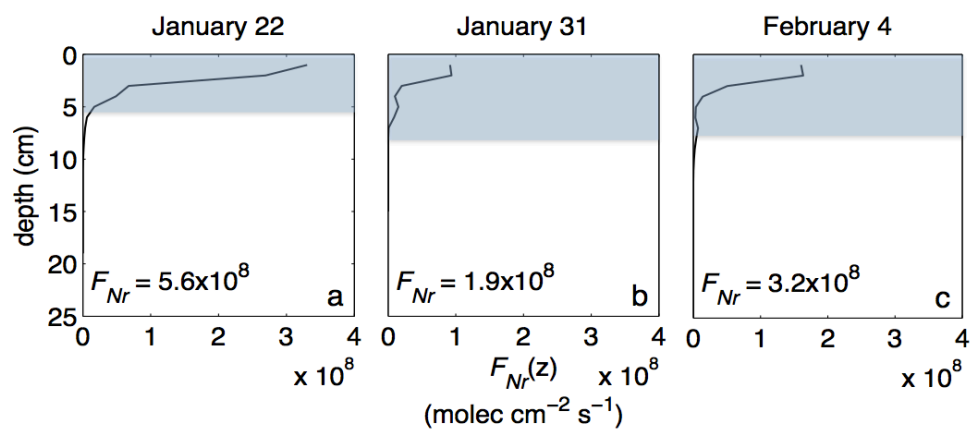
(molec cm^{-2} s^{-1})

1224
1225 Figure 5. Modeled vertical profiles of snow-sourced N_r fluxes (F_{Nr}, molec cm^{-2} s^{-1})
1226 calculated using E8. Also shown is total F_{Nr}, which is the depth-integrated F_{Nr} over the
1227 photic zone. The blue shaded region represents the snow photic zone.
1228
1229
1230
1231
1232
1233

Atmospheric
Chemistry
and Physics
Discussions
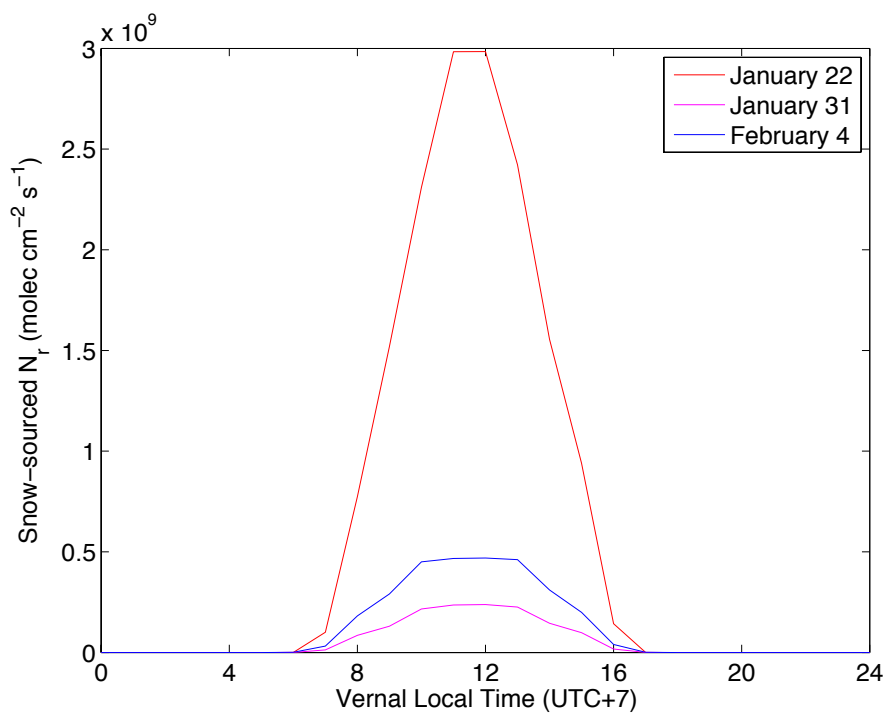
1234
1235 Figure 6. Modeled diurnal profiles of snow-sourced N_r fluxes (F_{Nr}, molec cm^{-2} s^{-1})
1236 calculated using TRANSITS on January 22 (red), January 31 (magenta), and February 4
1237 (blue).
1238
1239
1240
1241
1242
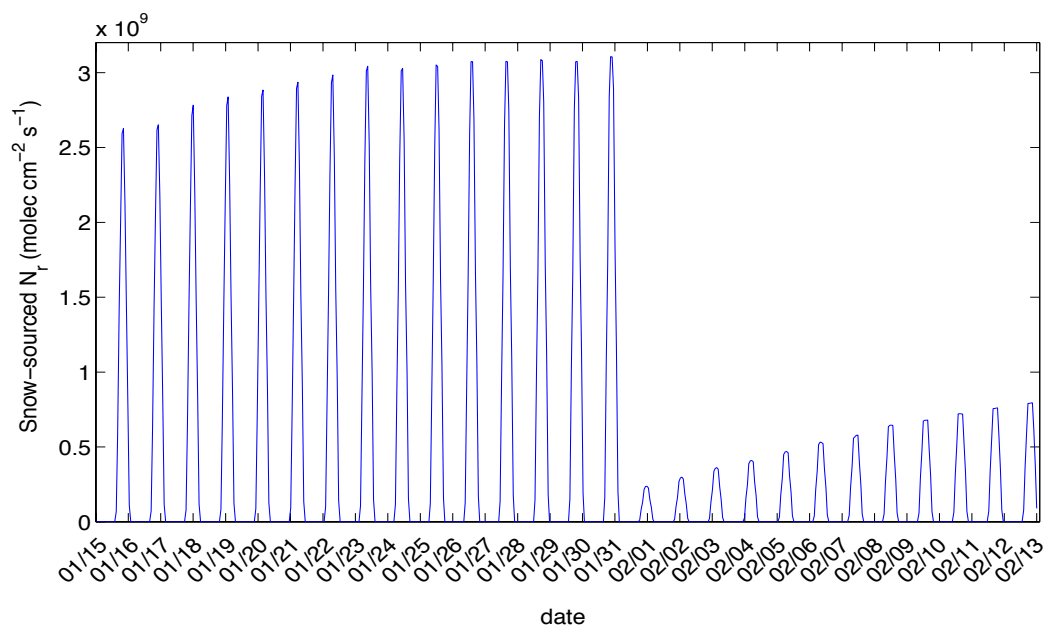
1243
Figure 7: Modeled snow-sourced N_r fluxes (molec cm^{-2} s^{-1}) for each hour during the
1244
1245   campaign from January 15 to February 11.
1246
1247

Atmospheric
Chemistry
and Physics
Discussions

Open Access
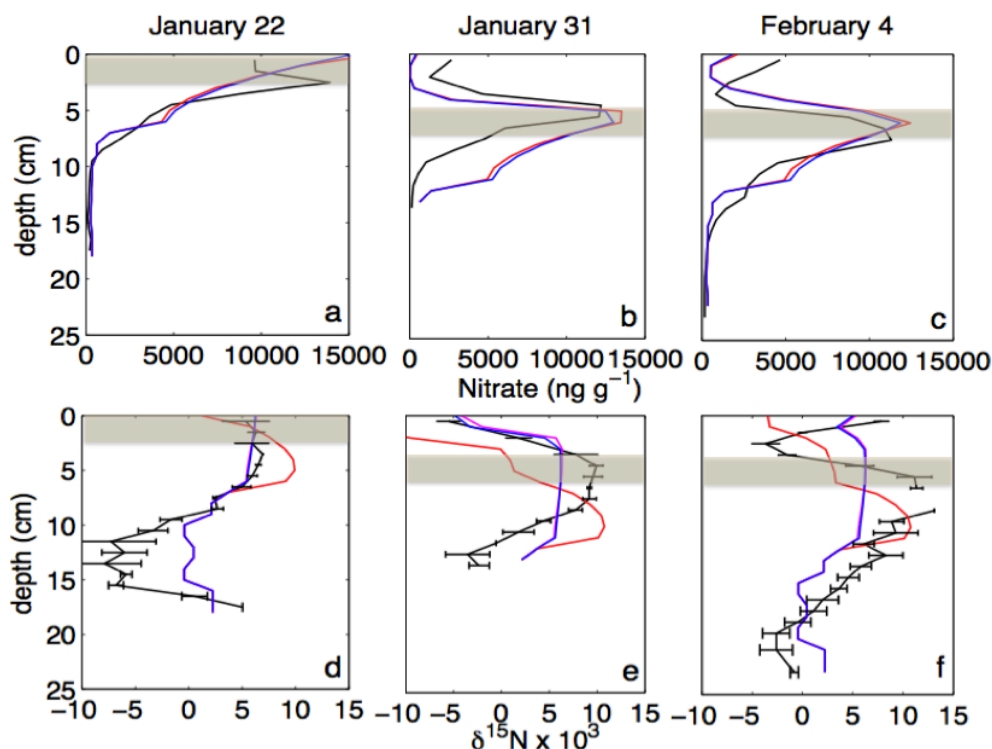
1248
1249 Figure 8. Measured (black) and modeled ($\Phi=4.6\times10^{-3}$, blue; $\Phi=0.2$, red) vertical profiles
1250 of snow nitrate concentration (top) and $\delta^{15}N(NO_3^-)$ (bottom) on January 22 (left), January
1251 31 (center), and February 4 (right). Modeled $\delta^{15}N(NO_3^-)$ profiles are calculated using
1252 variable quantum yields ($\Phi=4.6\times10^{-3}$, blue; $\Phi=0.2$, red, $\Phi=0$, magenta). The brown
1253 shaded region represents the dusty layer.
1254